



HAL
open science

Strength, fatigue strength and toughness of dissimilar Ti17–Ti64 linear friction welded joints: Effect of soft surface contamination and depletion of α precipitates

J.M. García, V.A. Esin, Thilo F. Morgeneyer

► To cite this version:

J.M. García, V.A. Esin, Thilo F. Morgeneyer. Strength, fatigue strength and toughness of dissimilar Ti17–Ti64 linear friction welded joints: Effect of soft surface contamination and depletion of α precipitates. *Materials Science and Engineering: A*, 2021, 799, pp.139989. 10.1016/j.msea.2020.139989 . hal-02938894

HAL Id: hal-02938894

<https://hal.science/hal-02938894>

Submitted on 5 Nov 2020

HAL is a multi-disciplinary open access archive for the deposit and dissemination of scientific research documents, whether they are published or not. The documents may come from teaching and research institutions in France or abroad, or from public or private research centers.

L'archive ouverte pluridisciplinaire **HAL**, est destinée au dépôt et à la diffusion de documents scientifiques de niveau recherche, publiés ou non, émanant des établissements d'enseignement et de recherche français ou étrangers, des laboratoires publics ou privés.

Strength, fatigue strength and toughness of dissimilar Ti17-Ti64 linear friction welded joints: effect of soft surface contamination and depletion of α precipitates.

GARCIA J.M., ESIN V.A., MORGENEYER T.F.

MINES ParisTech, PSL University,

Centre des Matériaux CNRS UMR 7633, BP 87 91003 Evry, France

Published in : Materials Science and Engineering:A. Volume 799, 2 January 2021, 139989.

DOI : <https://doi.org/10.1016/j.msea.2020.139989>

Correspondence

Juan Manuel García

MINES ParisTech, PSL University, Centre des Matériaux. (CNRS UMR 7633), BP 87 91003, Evry, France.

Email: jmgarcia.engineering@gmail.com

Funding information: *Agence Nationale de la Recherche* (Project number: ANR-14-CE27-0017).

Abstract

The effect of microstructure of three dissimilar Ti17–Ti64 linear friction welded joints on the strength, fatigue strength and fracture toughness was studied. A special attention was paid to role of soft contaminants and α precipitate depletion. Three joints were produced: one in the as machined state after electrical discharge machining, one ground prior to welding, and one welded in the as machined state and *post*-weld heat treated. The microstructure of the weld centre zone (WCZ) exhibited an acicular entangled α' martensite with a Widmanstätten morphology on the Ti64 side and fine equiaxed distorted β grains on the Ti17 side. A depletion of the strengthening α precipitates was observed in the WCZ and the thermo-mechanically affected zone (TMAZ) on the Ti17 side. For the studied welding parameters, the LFW self-cleaning mechanism failed to extrude the contaminants in the weld interface of the joint welded in the as machined state. These contaminants were related to prior to welding machining and were denominated soft contaminants due to their relatively low melting point. A defect layer was formed that led to a pseudo-brittle fracture in at the WCZ during tensile testing, cyclic loading and fracture toughness testing. During tensile testing of the joint that was ground prior to welding, failure occurred sometimes at the Ti64 parent material (PM) and sometimes at the

Ti17 TMAZ. Fatigue cracks initiated at the latter weak zone with a reduced fatigue strength. Compared to the PM, fracture toughness of samples even without fatigue pre-crack was also reduced. Failure at the weak zone highlighted unexpected colonies of elongated dimples that nucleated on transgranular deformation bands.

Keywords

Linear friction welding; defects; mechanical properties; Ti-5Al-2Sn-2Zr-4Cr-4Mo; Ti-6Al-4V; Ti17; Ti64.

Nomenclature

α (h.c.p.), hexagonal closed packed titanium crystal lattice; β (b.c.c.), body centred cubic titanium crystal lattice; α' (h.c.p.) acicular entangled martensite showing a Widmanstätten morphology; F , friction axis; P , pressure axis; T , thickness axis; E , Young's modulus; Y , yield strength; UTS, Ultimate Tensile Strength; $\varepsilon_{\text{macro}}$, macroscopic engineering strain; ε_{PP} , local strain following the P axis; $\dot{\varepsilon}_{\text{PP}}$, local strain rate following the P axis; σ_{max} , maximum fatigue stress; R , fatigue stress ratio; N_f , fatigue life; ΔK , stress intensity factor range; a , crack size; da/dN crack growth rate.

1 Introduction

The utilisation of titanium alloys is widespread in the aerospace industry. Their corrosion resistance, strength/density ratio and their ability of working at high temperatures make them one of the most used high performance materials. Aircraft components with intricate geometries are exposed to heavy and complex loadings in very aggressive environments. In aero-engines for instance, compressors are required to be manufactured with disks exhibiting high resistance for both tensile strength and low cycle fatigue and with blades exhibiting good resistance to high cycle fatigue and creep [1, 2]. This mixed requirement is commonly addressed by the assembly of different materials using innovative joining techniques, such as the fabrication of the so-called "Blisks": A blade made of Ti-6Al-4V assembled to a disk made of Ti-5Al-2Sn-2Zr-4Mo-4Cr by the use of Linear Friction Welding (LFW) [1, 2].

The Ti-6Al-4V is an α/β alloy commonly known as Ti64. For the study presented herein, its microstructure contained 10 μm diameter α grains and $\alpha + \beta$ colonies with large macrozones sharing similar crystallographic orientations to an extent of roughly 100 times the apparent grain size [3, 4, 5]. Ti64 exhibits good creep resistance up to a temperature of about 400 °C [6] and a low resistance to

crack propagation during the stage I fatigue regime [3, 7]. Ti64 was patented by Stanley [8] at the end of the 1950s and it still accounts for about 50% of the world titanium tonnage and up to 80% of the aerospace industry applications [9].

Ti-5Al-2Sn-2Zr-4Cr-4Mo, also known as Ti17, is a β -metastable titanium alloy known for its deep hardenability, good fracture toughness and fatigue crack growth rates [10, 11]. Its microstructural features consists in large β grains namely 500 μm in diameter containing different kinds of α precipitates: grain boundary, Widmanstätten lath colonies growing from the grain boundary and two kinds of Widmanstätten laths inside the β grains (primary and secondary). Ti17 was invented in 1973 by General Electric for its utilization in fans and compressor discs [9, 12].

LFW is a solid-state joining process in which a stationary workpiece, namely the disk, is put in contact with a second workpiece, i.e. the blades, describing an oscillatory motion of frequency f and amplitude a . After a fraction of a second of friction, a forging pressure P is applied to attain a target axial shortening Δh (burn-off). The plastic deformation and localized heat generated in the weld interface lead to considerable levels of residual stresses [13, 14], microstructural changes [15, 16, 17] and, sometimes, enhanced mechanical properties [18]. As a final consequence, all these features create considerable heterogeneities distinguished in four distinct zones : the WCZ, the TMAZ, the heat affected zone and the PM. This technique was first suggested by the patents of Ritcher [19], Chudikov [20] and Maurya and Kauzlarich [21] and it presents several advantages such as fast welding, reduced milling operations, the conception of dissimilar welds and, particularly, of having a self-cleaning mechanism at least to some extent [22].

A considerable wealth of literature concerning the tensile behaviour of dissimilar Ti17-Ti64 LFW joint is available. For the documented LFW configurations, failure under monotonic loading occurs in the Ti64 PM meaning that both Ti17 and the WCZ exhibit relatively higher strengths in the welded structure [1, 2, 23, 24]. These failure locations are in agreement with the specifications for the design of Blisks. Nonetheless, due to the hot deformation experienced during LFW, Ti17 undergoes a depletion of the α precipitates at the vicinity of the WCZ that induces some softening [15]. A similar depletion was observed for Ti17 and Ti5553 LFW joints [25, 26, 27], in which failure occurred at the TMAZ, suggesting that this location is a potential mechanically weak zone. The effect of these mechanically weak zones on the strength, fatigue strength and fracture toughness of dissimilar Ti17-Ti64 LFW joints has not previously been studied.

LFW is a solid state joining process [19, 21, 28, 29] known to be self-cleaning [30, 31]. Yet, several authors clean the workpieces prior to welding [23, 32, 33, 34] and nevertheless, the presence of impurities and welding defects have previously been reported [32, 33]. Optimized welding parameters

favour the effective extrusion of contaminants outside the weld interface into the flash [35]. Several authors have studied this issue by the use of numerical tools [36, 37, 38, 39]. Tracking points in the weld interface are followed during simulations of the welding process to determine the efficiency of the welding parameters in terms of contaminants removal. These approaches have given valuable insight about the self-cleaning mechanism of LFW. For instance, increasing the burn-off enhances the proper extrusion of contaminants in the weld interface [38]. However, their limitation seems to be that the PM tracking points do not necessarily model the physics of impurities, namely their melting temperature. Although hard contaminants are often observed in the weld interface of LFW joints, such as the α precipitates observed in near- α alloys [35], soft contaminants with melting temperatures lower than the temperature developed during friction can sometimes be found [22]. Non industrial machining techniques such as electrical discharge machining can lead to the presence of such contaminants, which can cause severe detrimental consequences for the mechanical properties of LFW joints. For instance, ductility reduction [40] or severe shortening of fatigue lifetimes [22] have been observed. A better understanding of the consequences on the mechanical properties of LFW joints of these soft contaminants is required.

Ti17 undergoes softening during LFW. The depletion of the α precipitates favours the formation of microstructures consisting in fine equiaxed distorted β grains and deformed β grains at the WCZ and TMAZ, respectively [15]. Microhardness profiles across the WCZ of similar LFW joints of β titanium alloys revealed their undermatching strength [15, 25, 41]. Li et al. [25] carried out a study on the tensile properties of a similar Ti17 LFW joint and found out that, for one specimen, failure occurred at the TMAZ exhibiting reduced macroscopic strain and ultimate tensile strength compared to the PM. The authors observed elongated damage features in the fractographs that were attributed to the brittle fracture at the TMAZ. The same depletion of the α precipitation led to poor mechanical properties of similar Ti5553 LFW joints [26, 27]. It seems clear that the depletion of the α precipitates at the WCZ and TMAZ represents a structural weakness for similar Ti17 and Ti5553 LFW joints. Nevertheless, a sound explanation about the phenomena leading to failure at these weak zones and its underlying mechanisms is still missing in the literature.

In this work, the mechanical properties in terms of microhardness, tensile strength, fatigue strength and fracture toughness of dissimilar Ti17-Ti64 LFW joints were studied for three blocks: one, welded after cutting by electrical discharge machining without any additional surface preparation; a second, welded in the as machined condition and post-weld heat treated, and a third, ground prior to welding. First, a microstructural characterization of the joints is carried out using energy-dispersive X-ray spectroscopy and electron backscattered diffraction analyses. Second, the tensile behaviour of all joints is compared. An assessment of the strain and strain rate obtained by stereo digital image

correlation instrumentation of the tensile tests is performed to identify the fracture location on the welded structure. Third, the fatigue strength, the fatigue crack initiation and propagation of the cross-welded specimens are studied. Fourth, results of fracture toughness testing, sometimes without fatigue pre-cracking, of non standard specimens, are presented. The consequences of contaminants in the weld interface produced by prior to welding electrical discharge machining and the potential threat to the welded structure integrity given by the mechanically weak zones are discussed here.

2 Experimental & Materials

2.1 Parent materials

Ti17 and Ti64 titanium alloys were used as PM in this study. Their PM nominal and measured chemical compositions are shown in Table 1. The measured chemical composition were provided courtesy Timet. The chemical composition for Ti17 and Ti64 were measured using X-Ray Fluorescence Spectroscopy and inductively coupled plasma mass spectrometry, respectively. The microstructures of both parent materials are shown in Figure 1. The microstructure of Ti17 consisted of 550 μm diameter prior- β grains containing α laths in four forms: grain boundary α (α_{GB}), Widmanstätten lath colonies grown from the grain boundary (α_{WGB}) and two kinds of Widmanstätten laths precipitates inside the β grains (primary α_{WI}^p and secondary α_{WI}^s). The α_{WI}^p precipitates had lengths and widths of respectively 4.4 μm and 1.6 μm [15]. Ti64 presents a bimodal α/β microstructure containing α grains of about 10 – 20 μm in diameter with a colony-type lamellar matrix of alternating α and β plates. The β -transus temperatures of Ti17 and Ti64 respectively are 888 °C and 996 °C.

Table 1: Parent materials' chemical composition (%wt.). (*) The chemical composition measurements were carried out using X-Ray Fluorescence Spectroscopy for Ti17 and inductively coupled plasma mass spectrometry for Ti64 and were provided courtesy of Timet.

Ti17	Al	Sn	Zr	Mo	Cr	Fe	C	O	N	Y	B	Cu	Mn
Nominal	5	2	2	4	4	-	-	-	-	-	-	-	-
Measured(*)	5	1.99	2.03	4.10	3.98	0.04	0.0055	0.1107	0.0022	<0.0010	<0.001	<0.002	<0.005
Ti64	Al	V	Fe	C	O	N	Y						
Nominal	6	4	-	-	-	-	-						
Measured(*)	6.36	4.14	0.15	0.02	0.20	0.004	<0.0005						

The alloys were provided by Timet in the form of 250 mm diameter billets. Blocks with 80 mm \times 70 mm \times 15 mm dimensions were machined using electrical discharge machining. The long direction of the blocks coincided with the extrusion axis of the billet. The cutting tool was a brass wire

composed of zinc and copper.

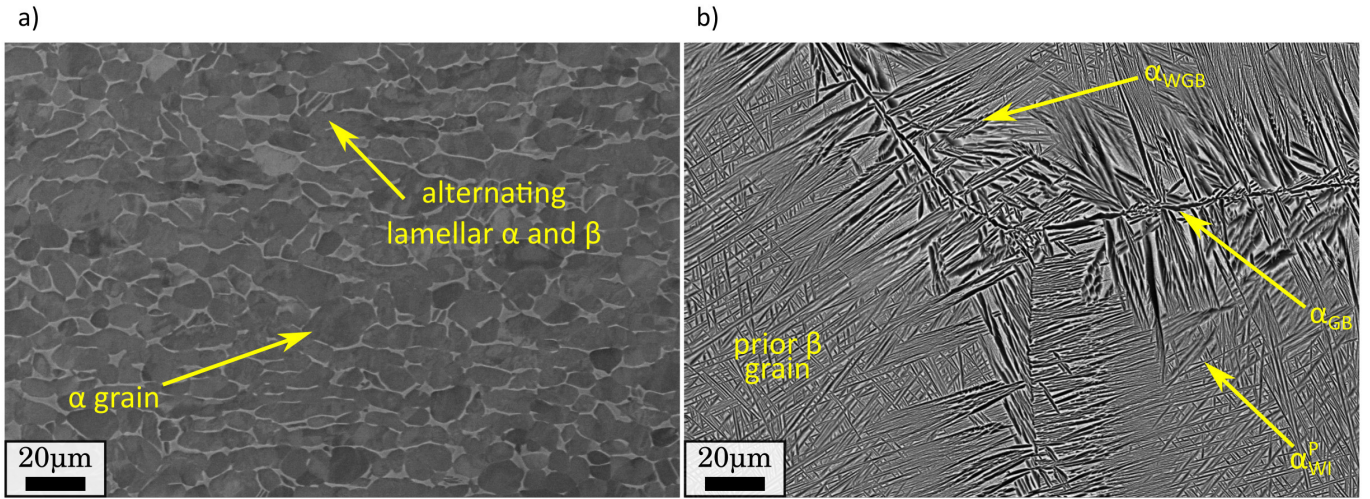


Figure 1: SEM/BSE observations of the microstructure of the a) Ti64 and b) Ti17 PMs.

2.2 Linear Friction Welds

Dissimilar Ti17-Ti64 LFW joints were provided by ACB. The Ti17 and Ti64 blocks were used as the stationary and oscillatory workpieces, respectively. During welding, friction occurred parallel to the F axes and the forging pressure was applied along the P axes, as shown in Fig.2. The third direction was the thickness (T). The F and P axes were parallel to the long and short directions of the blocks, respectively. Welding was performed with friction and forging pressures of $P = 90$ MPa, a frequency of oscillation of $f = 50$ Hz, an amplitude of oscillation $a = 2$ mm and a burn-off $\Delta h = 5$ mm. The average welding time was about $\Delta t = 3.075$ s. The blocks were degreased using an acetone bath prior to welding. Three dissimilar Ti17-Ti64 LFW joints were produced and are detailed in Table 2.

Table 2: Studied configurations of dissimilar Ti17-Ti64 LFW joints.

Designations	Description
as welded	PM blocks welded in the as machined state.
as welded–heat treated	PM blocks welded in the as machined state and post weld heat treated.
ground–welded	PM blocks welded after grinding for 2 min using a 1200 grit SiC paper.
PM	Parent materials.

The *post*-weld heat treatment applied consisted in an isothermal hold at 910 °C for 3 h in vacuum followed by a 2 h cooling down to 635 °C. After ageing for 8 h, the joint was air cooled.

2.3 Microstructure characterization

Standard procedures were used for the metallographic sample preparation: mounting, grinding and polishing to a mirror like finish. Microstructural observations were carried out in a ZEISS Sigma 300 Scanning Electron Microscope (SEM) operated at 15 kV using backscattered electrons (BSE) detector. The fractographic analysis was accomplished at low and high magnification using a secondary electron (SE) detector.

The chemical composition was investigated using Energy-dispersive X-ray spectroscopy (EDX) for metallographic specimens machined from the PM blocks and the LFW joints. Samples were plated in nickel strike baths at room temperature for 3 min. EDX analyses were performed in a ZEISS Sigma 300 Scanning Electron Microscope operated at 20 kV.

Characterization using Electron Backscattered Diffraction (EBSD) was performed to obtain an insight into the different mechanisms related to welding. EBSD mappings were carried out using a camera Nordif UF300 of $840 \text{ px} \times 840 \text{ px}$ with a step size of $0.5 \mu\text{m}$. Samples were ground using an Leco PX500 automatic polisher. After grinding, the mirror like quality was achieved by polishing using a solution composed of 200 mm^3 Struers oxide polish suspension and 200 mm^3 distilled water for 24 h on a Buehler VibroMet. No etching was performed. The working distance for EBSD acquisition was 24 mm. The voltage was set to 20 kV. A minimum grain size of 5 px and a minimal confidence coefficient of 0.2 filters were applied.

2.4 Mechanical characterization

Microhardness Tests were conducted according to the ASTM E384-17 [42] standard. Vickers microhardness profiles parallel to the P direction were carried out across the WCZ. The step size was $200 \mu\text{m}$, the load was 500 g and the dwell period was 15 s.

Tensile test Tensile tests were conducted according to the ASTM E8/E8M-16a [43] standard. Three sets of cross-weld tensile specimens were machined from the three LFW joints described in Table 2. The geometry of the tensile specimens is shown in Fig. 2b. The tensile test specimens were machined parallel to a PT plane and were tested having their principal axis parallel to the P direction. Load was applied with a MTS 250 kN load frame at room temperature. Typical gauge length and cross section respectively were 25 mm and $3 \text{ mm} \times 6 \text{ mm}$. Elongation was measured with optical extensometers as described later in this Section. Load frame cross-head speed was 0.032 mm s^{-1} .

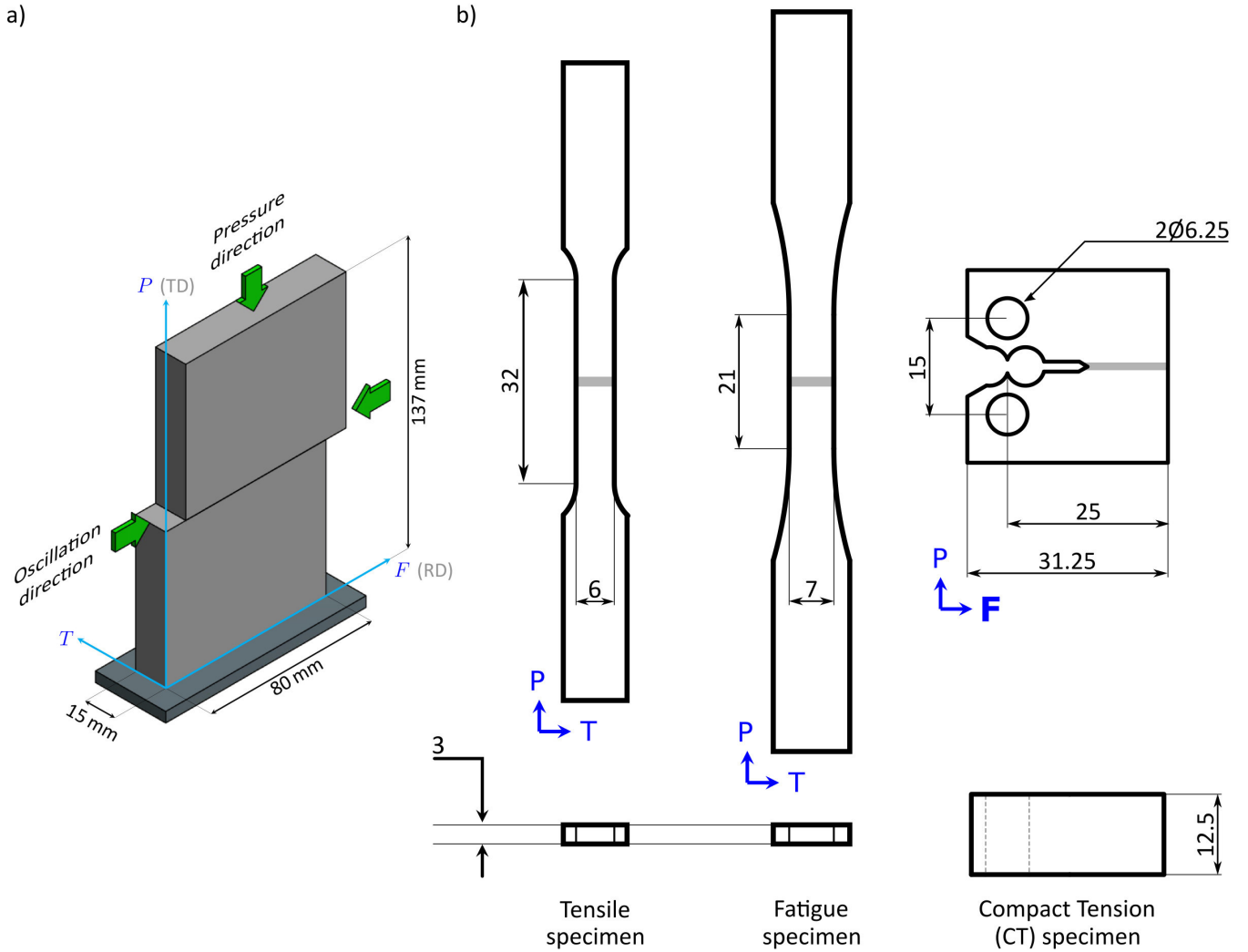


Figure 2: a) Schematic view of the welded joint showing the friction direction (F), the forging pressure direction (P) and the thickness direction (T) and b) geometry of the tensile, fatigue and fracture toughness specimens. All dimensions are given in mm.

Stereo Digital Image Correlation During tensile testing, the local strain over the tensile specimens surface was monitored using a standard system of stereo digital image correlation. A system of two 2048 px \times 2048 px Manta G-419B cameras was placed to follow the displacement of an artificial random black and white speckle applied on the specimen surface. The distance between the cameras was $a = 26$ cm and the camera-object distance was $b = 31$ cm, leading to a field of view of 40 mm \times 40 mm. Images were exploited with Vic-3DTM from Correlated Solutions, Inc. (version 7.2.4, 2014). Acquisition was carried out taking 2 frames per second. Subset size was 35 px \approx 175 μ m, step size was 9 px and filter size was 15 px. Before tensile testing, the displacement and the Hencky ε_{PP} measurements uncertainty were determined by correlating two consecutive images of the static specimen. Uncertainty in displacement measurements was 0.1 μ m. This corresponds to a Hencky strain uncertainty of $\Delta\varepsilon_{PP} = 0.0002$ with a standard deviation of $\sigma_{\varepsilon_{PP}} = 9.56 \times 10^{-5}\%$. The load line, the specimen and the cameras frame were aligned using a laser level as a reference. Both cameras

were aligned to gravity using a water level.

Fatigue test Standard fatigue tests were carried out according to the ASTM E 466-07 [44] standard. The load frame was aligned following the procedure described by García and Morgeneyer [45]. Smooth cross-weld specimens were machined parallel to a PT plane of the joint, having their principal axes parallel to the P direction, as shown in Fig.2b. Specimens' corners were rounded with a file and their surfaces were polished to a mirror-like state. The uniaxial tension zone had a length of 21 mm and a constant gauge section of $3\text{ mm} \times 7\text{ mm}$. A sinusoidal waveform was imposed using a MTS 250 kN servo-hydraulic load frame. The test frequency was 20 Hz. The target fatigue life was $N_f = 10^5$ cycles with a stress ratio of $R = 0.1$.

Fracture toughness Compact Tension (CT) specimens were machined according to the ASTM E1820-08 [46] standard. The specimen geometry is shown in Fig.2b. All specimens were machined with thickness of $B = 12.5\text{ mm}$ to assure a crack propagation under plane strain and notch of $h = 11\text{ mm}$. The CT cross-weld specimens were machined parallel to a FT plane with the crack propagation parallel to the F direction. The crack of the cross-weld CT specimens was precisely centred with respect to the WCZ. The target pre-crack extension was $f = 1.5\text{ mm}$ and it was performed under force-controlled fatigue. The pre-crack extension was monitored on both sides of the specimen. The pre-crack extension of each CT specimens is indicated on each graph of Fig.14. The pre-crack that respected the standard requirements are written in green and the pre-crack for the invalid tests is written in red. Detailed information concerning the validity of each trial is detailed in Section 3.5. Fracture toughness tests were performed using three specimens of Ti17 PM (with pre-cracks), one specimen of the as welded LFW joint (without pre-crack) and two specimens from the ground-welded LFW joint (one with a pre-crack and one without a pre-crack). Tests were carried out applying a displacement-controlled loading on an Instron 8500 load frame with a load ratio of $\dot{K}_{Ic} < 2.75\text{ MPa}\sqrt{\text{m}}/\text{s}$, as recommended by the standard. Force and crack mouth opening displacement (CMOD) were simultaneously recorded during the test for the evaluation of the stress intensity factor as a measure of the fracture toughness. CMOD was measured with an MTS 632,02F-21 extensometer. A pre-load of 0.2 kN was applied to every specimen prior to testing. Fracture toughness specimens were etched *post-mortem* with a Kroll's 2 reagent ($12\%\text{HF} + 18\%\text{HNO}_3 + 70\%\text{H}_2\text{O}$) to identify failure location and to study damage nucleation by SEM observations.

3 Results

3.1 Microstructure characterization

3.1.1 Flash morphology and weld microstructure of the ground-welded LFW joint

A cross-weld optical observation along a PT plane of the ground-welded LFW joint is shown in Fig.3a. Ti17 and Ti64 can be respectively seen on the upper and lower parts of the weld. The flash for the Ti17 and Ti64 sides respectively show a length of about 10 mm and 25 mm. No ripples can be observed for either material. The optical observation of the out-of-plane flash, while not conclusive, suggests that the power input used here led to sufficient softening of both materials and enhanced the continuous extrusion of impurities in the weld interface.

The strong contrast in the SEM/BSE observations of Figs.3b and 3c was provided by the chemical content of each material. In Fig.3b, the frontier between both materials at the WCZ and their microstructures is clearly observed. Similarly, in Fig.3c, it can be observed that some mass of Ti17 penetrated in the Ti64 side. This phenomenon is well known in the LFW literature as material flow [37] but, in addition to this, some diffusion may occur. This is particularly important for a dissimilar Ti17-Ti64 joint because the alloying elements of each side of the weld are different. Thus, their diffusion may lead to more complex microstructure transformations than those observed in similar joints, i.e., in a similar Ti17 LFW joint. Nonetheless, since the material is exposed to high temperature for a very short period of time, the effect of diffusion is likely to be localized or neglectable. Henceforth, it seems reasonable to state that the microstructure transformation during joining is mostly influenced by the hot deformation undergone during joining. This is consistent with the similarity observed between the microstructure in each side of the WCZ and the microstructure of the similar Ti17 LFW joints and the similar Ti64 LFW joint respectively documented by Ballat-Durand et al. [15] and Wanjara and Jahazi [33]. For instance, the WCZ of the Ti64 side exhibits an acicular microstructure with a Widmanstätten morphology that is very similar to the one observed in similar Ti64 LFW joints [33]. This microstructure suggests that the temperature developed during welding locally was higher than the β -transus temperature. It seems that, during rapid cooling after the oscillations stopped, a displacive diffusionless transformation led to the formation of an acicular entangled α' martensite, such as the one observed in the hot deformation of α/β titanium alloys [47].

In addition, the 10 μm diameter features observed in the Ti17 side of the WCZ are very similar to the α depleted β distorted grains seen in the WCZ of the similar Ti17 LFW joints characterized by Ballat-Durand et al. [15], Dalgaard et al. [26] and Wanjara et al. [27].

A SEM/BSE observation of the Ti17 TMAZ is shown in Fig.3d. The graded yellow arrow shows the gradual depletion of the α phase that increases with decreasing distance from the WCZ. The green arrow in Fig.3d points to the former α_{GB} layer at the grain boundary of β grain at the Ti17 TMAZ. These features were that was previously denominated as “traces of $\alpha_{GB} + \alpha_{WGB}$ ” [15]. The region with a darker shade of grey represents the Ti17 TMAZ. This region recalls the TMAZ of the similar Ti5553 LFW joint studied by Dalgaard et al. [26], which was the location for failure during

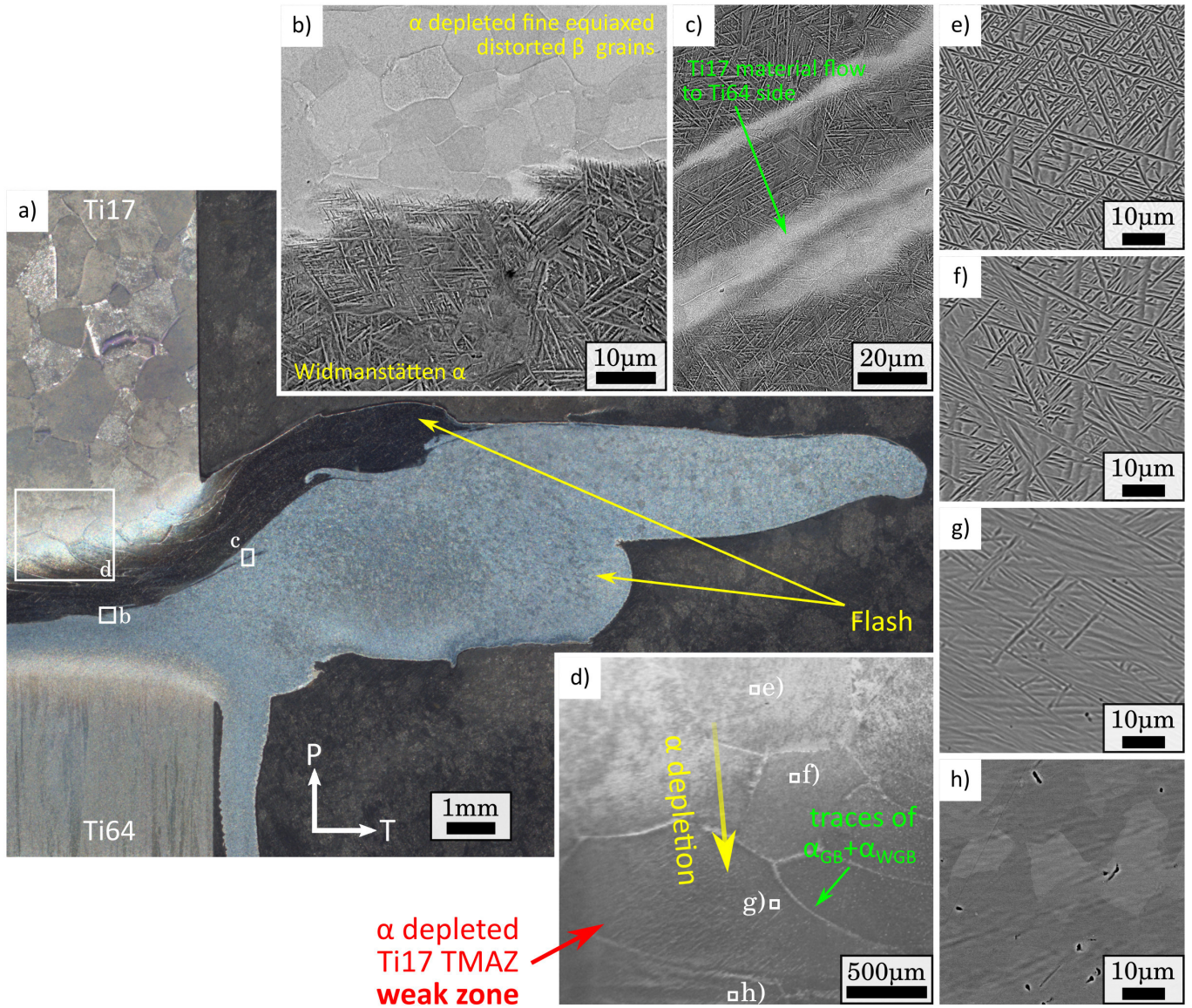


Figure 3: a) Cross-weld optical observation of the microstructure of the ground-welded LFW joint showing the PM, the TMAZ and the WCZ for both sides of the weld. The upper and lower parts of the weld respectively correspond to Ti17 and Ti64 PM's; b) observation of the WCZ showing α depleted fine equiaxed distorted β grains in the Ti17 side and the Widmanstätten morphology of the α' martensite in the Ti64 side; c) material flow of Ti17 into the Ti64 side of the WCZ and d) α depleted deformed β grains in the weak zone (Ti17 TMAZ). Zoomed regions of Fig.3d are shown in Figs.3e, 3f, 3g and 3h.

monotonic loading.

3.1.2 Analysis of the defect layer at the WCZ of the as welded LFW joint

During the microstructural characterization of the as welded LFW joint, an unexpected defect layer was observed at the Ti17-Ti64 frontier, in the centre of the WCZ (see the SEM/BSE observation of Figs.4a and 4b). The defect layer exhibited a length of 1.8 mm over an observed surface of 3 mm length and thickness of about 11 μm (see Figs.4a and 4b). It exhibited round cornered objects and voids. These features do not convey the shape of microstructures commonly seen in the WCZ of LFW joints for either similar or dissimilar LFW joints made of Ti17 or Ti64. Similar voids were observed in the reports documented by García and Morgeneyer [22], Wanjara and Jahazi [33] and Ballat-Durand et al. [48].

To better characterize the defect layer, a chemical composition profile obtained by EDX analysis over the transparency white arrow of Fig.4b is shown in Fig.4c. The alloying elements included in the analysis were those of both PM's (see Table 1) plus Cu, Zn and O. V is found on the nominal composition of Ti64 however some concentration of V can be observed in the Ti17 side of the defect layer. Similarly, low concentrations of Sn, Zr, Mo and Cr are to be seen on the Ti64 side of the defect layer, given that they belong to the nominal composition of Ti17. Whilst Ti64 and Ti17 respectively contain 6 %wt and 5 %wt of Al in their nominal compositions, the defect layer exhibited a concentration of about 3.8 %wt. Furthermore, about 6.25 %wt of O was observed at the defect layer. These trends are also observed on the chemical composition mappings of Fig.4d. The O concentration observed over the entire region can be explained by the fact that titanium alloys develop an oxide layer almost instantaneously when in contact with the atmosphere. Nevertheless, it is very interesting to note that the concentration of O is higher at the defect layer (see Fig.4c). The defect layer contains significant amounts of Ti, Al and O and it is surrounded by Cu and Zn gradients that decrease with increasing distance to the defect layer.

García and Morgeneyer [22] suggested that the brass wire used for electrical discharge machining prior to welding may have smeared the surfaces of the PM's blocks with significant amounts of Cu or Zn. To confirm this, the chemical content of PM blocks prior to welding was studied through EDX mappings. SEM/BSE observations of the surface of two PM blocks are shown in Figs.4e and Fig.4f (read Section 2.1). An EDX mapping showing the %wt content of Cu is highlighted in red. The microstructure of both PM's is easily recognized. Astonishingly, an undesired layer containing a maximum of 8 %wt of Cu was observed in the surfaces to be welded. This confirms that, during electrical discharge machining, the brass wire smeared the surfaces to be welded with substantial

amounts of Cu. These findings highlight that the as welded LFW joint was produced with PM's blocks containing surface contamination.

An EBSD orientation map and a phase map of both α and β phases are respectively shown in Fig.5a and Fig.5b. These maps correspond to the region highlighted by the white rectangle in Fig.4b. For both mappings, the indexation confidence index has been highlighted. Both the defect layer and the Ti64 side of the WCZ exhibit an hexagonal crystal lattice. The Ti17 side of the WCZ shows ~ 10 mm diameter β grains.

The transparency level highlights that the indexation confidence index varies in each region. It

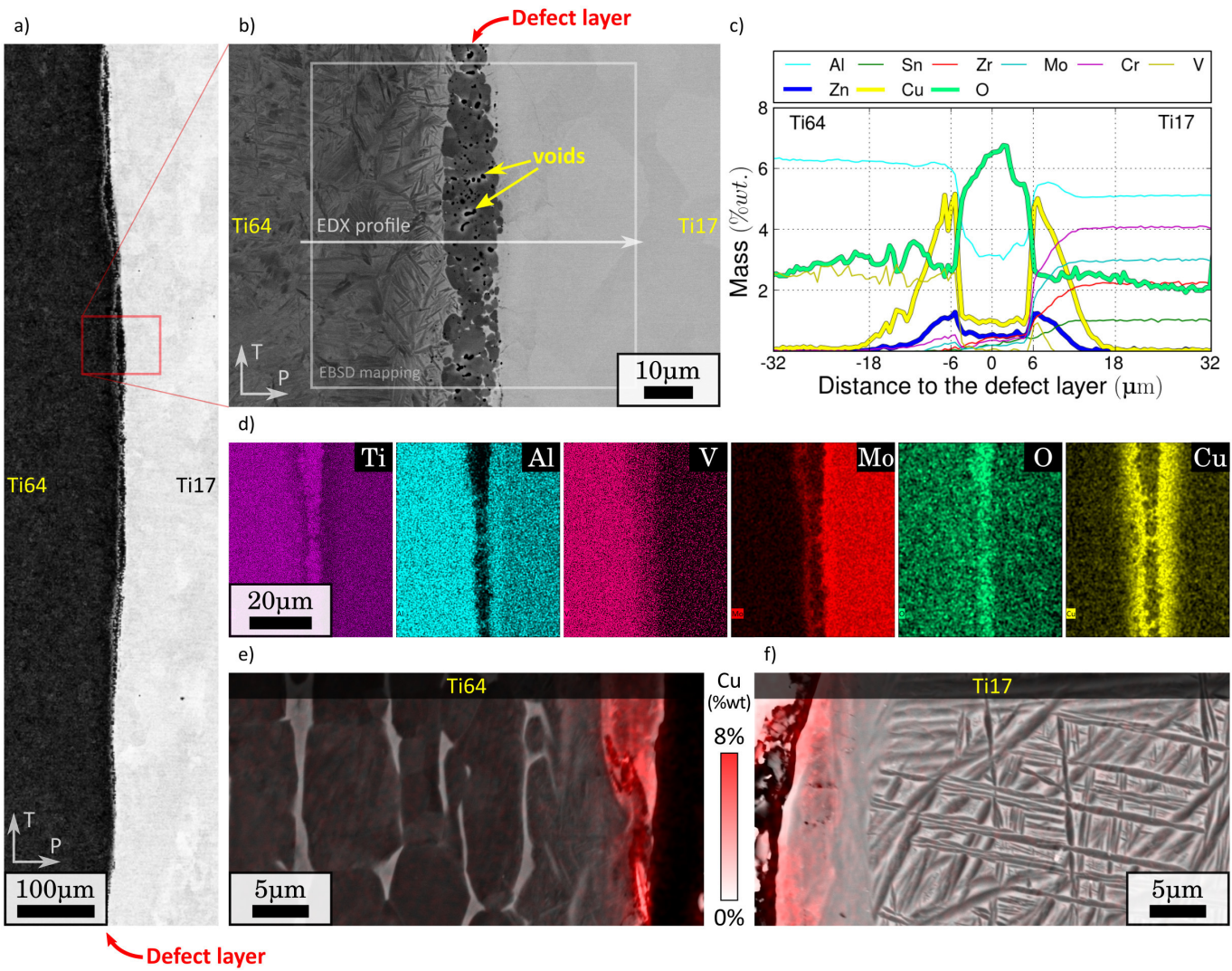


Figure 4: SEM/BSE observations of the as welded LFW joint at a) low and b) high magnifications, showing the defect layer containing round objects and voids ; c) chemical composition profile across the defect layer obtained by EDX analysis along the white transparency line on Fig.4b; d) chemical composition mappings of different chemical elements obtained by EDX analysis and prior to welding SEM/BSE observations with mappings of Cu content expressed in %wt highlighted in red for the PM's blocks: e) Ti64 and f) Ti17.

is a minimum for the Ti17 side of the WCZ and maximum for the defect layer. The lower confidence index on the β phase is attributed to the fact that the microstructure at the Ti17 WCZ consists of α depleted distorted β grains that exhibited slightly different crystal lattice parameters from standard titanium β [15]. On the Ti64 side, the Widmanstätten morphology already mentioned in Section 3.1.2 can be seen. It is interesting to note that, regardless of the presence of a defect layer, the recrystallization undergone by both PM seems to be the same as that observed for the ground-welded joint. The EDX analyses of Section 3.1.2 have shown that the defect layer was mostly composed of Ti, Al and O and contained some Cu and Zn. The EBSD analysis suggests that the crystal lattice of the defect layer is hexagonal closed packed. Identifying the microstructure of the defect layer with data shown here is rather difficult. A better precision concerning the crystallography of the defect layer could be obtained by transmission electron microscopy but considering the 11 μm thickness of the defect layer, this seems cumbersome and time consuming.

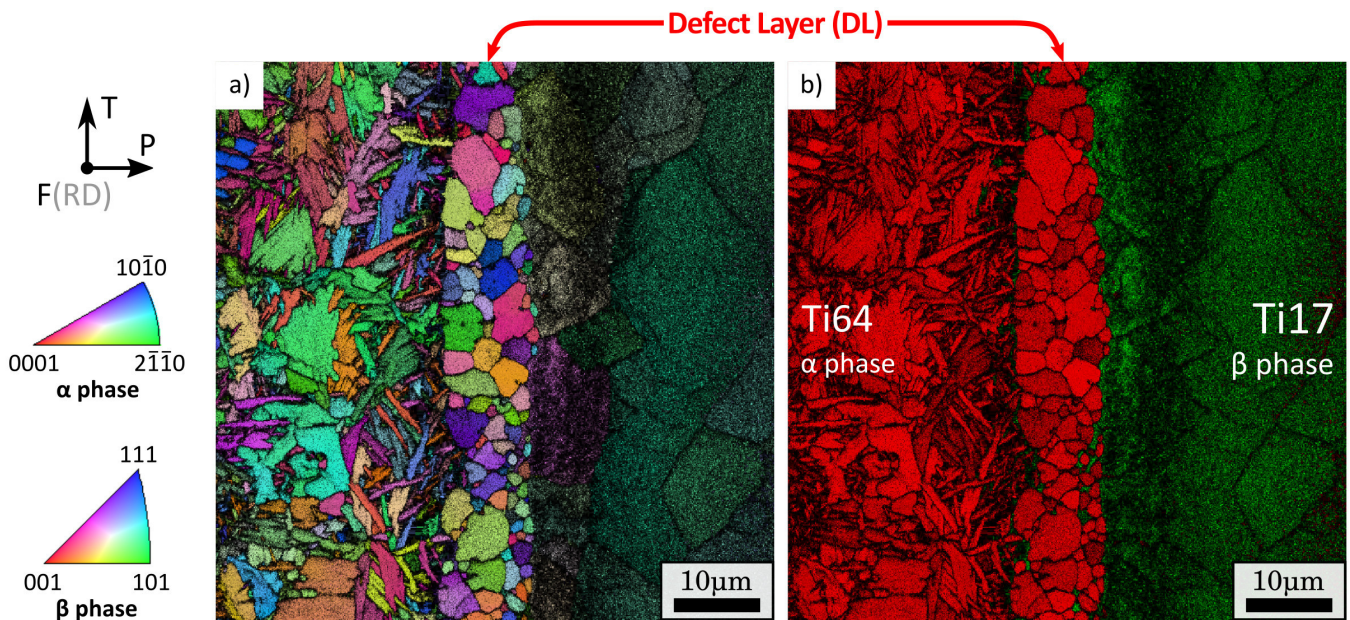


Figure 5: a) EBSD inverse pole figure of both α and β phases on the region framed by a white rectangle in Fig.4b showing the WCZ and the defect layer, and b) phase map respectively showing titanium α and β phases in red and in green. The indexation confidence index is overlaid for both maps.

This defect layer exhibited an hexagonal closed packed crystal lattice and was observed to be rich in Ti, Al and O and it is surrounded by Cu and Zn gradients that decrease with increasing distance to the defect layer. The high content in O and the grains morphology of the defect layer suggest that it might be an oxide layer. Another plausible interpretation is that the defect layer may have favoured the diffusion of the others elements [49] and have induced the formation of a brittle phase known as α -case [50]. Below, it will be shown that the defect layer is very detrimental for

the mechanical properties and that it can be easily avoided by a proper prior to welding surface preparation. Hence, a deeper investigation on the nature of this defect layer is not conducted here.

3.2 Microhardness

Fig.6 shows microhardness profiles across the weld for the three configurations. Profiles are parallel to the P direction. The microhardness profiles are respectively plotted in green, red and black for the as welded, the ground-welded and the joint welded-heat treated LFW joints. For all configurations, microhardness exhibited a local maximum of 380 HV at $P = 0$ mm and a gradual decrease to the Ti64 PM. Both the as welded and the ground-welded LFW joints exhibited local minima at the TMAZ of the Ti17 material. These findings are in agreement with the results already registered in the literature [23, 51]. Furthermore, the local decrease of microhardness at the TMAZ on the Ti17 side is consistent with the α depleted β grains in the TMAZ of similar Ti17 LFW joints documented elsewhere for similar Ti17 LFW joints [15, 25, 26, 41]. After the heat treatment, microhardness of the Ti17 stabilized around PM's microhardness. The microhardness gradient on the Ti17 side was drastically sharper compared to the Ti64 side. The width of the affected zone was about 1 mm for the Ti64 side and 3 mm for the Ti17 side. One may state that the monotonic and cyclic failure locations should take place at the TMAZ on the Ti17 side or far on the Ti64 PM, given that these zones are softer. Moreover, it is interesting to note that the microhardness evolution of the as welded LFW joint was similar to the one of the ground-as welded joint which suggests that the defect layer described in Section 3.1.2 did not affect the microstructural evolution undergone by both PM during joining. The typical size of microhardness indentations was about 55 μ m. Nano-indentation could have provided further information about the mechanical properties of the 11 μ m width defect layer but since these properties are undesirable, the measurements were not carried out.

3.3 Monotonic tensile behaviour

The macroscopic engineering stress-strain curves of the tensile specimens for the as welded, ground-welded and welded-heat treated LFW joints are respectively plotted in green, red and black in the graph of Fig.7. The blue crosses depict failure for each curve. The tensile specimens coming from the as welded and welded-heat treated LFW joints failed in the elastic domain with very low deformation and a maximum engineering stress of about 560 MPa. This purely elastic deformation is not desirable for engineering applications. The tensile specimens of the ground-welded LFW joint showed some plastic deformation with significant scatter in the strain to failure. The tensile specimens ground-welded-1 and ground-welded-3 exhibited a mean UTS of 1050 MPa and failed

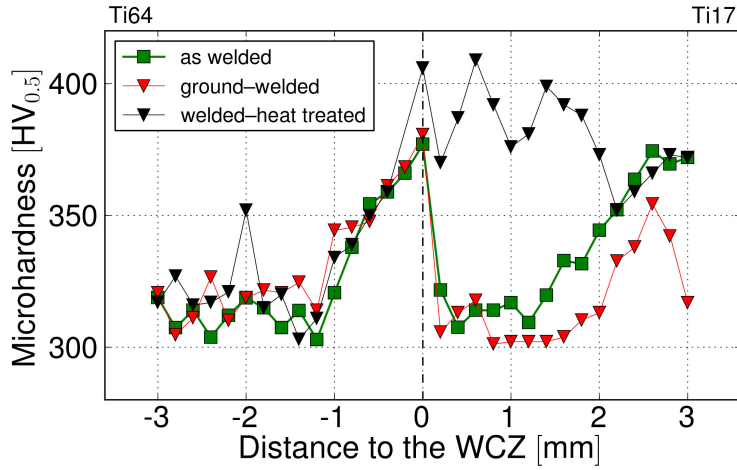


Figure 6: Microhardness profiles across the WCZ for the three configurations: the as welded (green), ground-welded (red) and welded-heat treated LFW (black) joints.

after significant deformation and some necking far from the WCZ at the Ti64 PM. The tensile specimens ground-welded-2 and ground-welded-4 failed with no necking at the UTS in the vicinity of the WCZ. In Section 3.3.1, it will be shown that failure occurred at the mechanically weak zone: the Ti17 TMAZ. Given that the tensile specimens are cross-welded structures, it would be interesting to track the location of the first stages of plastic activity and failure. Furthermore, it seems of primary interest to understand the origin of the scatter in strain to failure exhibited by the tensile specimens of the ground-welded LFW joint. These questions are approached in Sections 3.3.1 and 3.3.3.

The most outstanding fact is how detrimental the defect layer described in Section 3.1.2 can be for the tensile strength and plastic behaviour of cross-weld tensile specimens. It also should be noticed that the problem of contamination prior to welding cannot be solved by means of the thermal treatment. These findings suggest that the as welded and welded-heat treated joints may exhibit very poor behaviour in terms of fatigue and fracture toughness. To grind the surfaces machined by electrical discharge machining prior to LFW seems critical to obtain desirable mechanical properties.

3.3.1 First stages of plastic activity and failure location

The aim of this Section is to better understand the scatter in macroscopic strain to failure exhibited by the tensile specimens of the ground-welded LFW joint (see Section 3.3) and to measure the local strains in the different weld zones. To do this, the location on the welded structure of both the first stages of plastic activity and failure were studied by comparing the normalized strain rate fields obtained by stereo digital image correlation of the specimens that failed at the Ti64 PM and at the Ti17 TMAZ (see the graphs of the ground-welded-1 tensile specimen in Figs.8a-e and those of the ground-welded-2 tensile specimen in Figs.8f-h). The macroscopic tensile curves are plotted in the

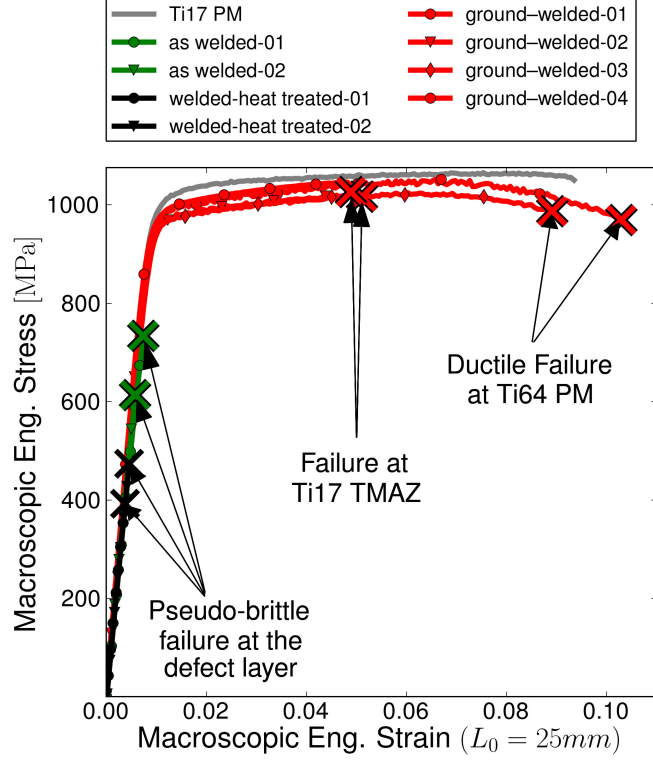


Figure 7: Macroscopic engineering stress-strain curves for the three configurations: the as welded (green), ground-as welded (red) and welded-heat treated (black) LFW joints.

graphs of Figs.8b, 8e, 8g and 8j having the macroscopic engineering strain in the horizontal axis and the macroscopic engineering stress in the secondary vertical axis. The overlaid numbers on the tensile curves correspond to the eight maps of cumulated strain ε_{PP} (see Figs.8a and 8f) and normalized strain rate $\dot{\varepsilon}_{PP}^{\text{norm}}$ fields (see Figs.8d and 8i).

The computation of $\dot{\varepsilon}_{PP}^{\text{norm}}$ was carried out as shown in Eq.1. Notice that $\dot{\varepsilon}_{PP}^{\text{norm}}$ is computed by normalizing the entire strain rate field with respect to the maximum strain rate found on the field, unlike the computation introduced by García and Morgeneyer [22], in which the normalization was performed with respect to the maximum strain rate found on the generatrix line. In the appendix A, the strain increment/strain uncertainty ratio is analysed to verify that the strain uncertainty associated to stereo digital image correlation is neglectable with respect to the strain increment used on the normalized the strain rate computation.

$$\dot{\varepsilon}_{PP}^{\text{norm}}(\varepsilon_{\text{macro}_i}; P) = \frac{\dot{\varepsilon}_{PP}(\varepsilon_{\text{macro}_i}; P)}{\max\{\dot{\varepsilon}_{PP}(P; T; \varepsilon_{\text{macro}_i})\}} \quad (1)$$

Each first map in Fig.8 corresponds to the domain of macroscopic elastic deformation and each second map has been taken after the onset of macroscopic plastic activity. The ε_{PP} and $\dot{\varepsilon}_{PP}^{\text{norm}}$ spatio temporal graphs (see Figs.8b, 8e, 8g and 8j) were constructed using the generatrix lines indicated in Figs.8d and 8i. The P coordinate along the generatrix lines has been set to match the location of the WCZ (see the white horizontal dashed lines on the maps and spatio temporal graphs). The

$\dot{\epsilon}_{PP}^{\text{norm}}$ spatio-temporal graphs for the ground-welded-1 and ground-welded-2 tensile specimens are respectively plotted in Figs.8g and 8j. Each set of maps share the colour bar with their corresponding spatio-temporal graphs. *Post-mortem* views of the tensile specimens are exhibited in Figs.8c and 8h. The overlaid green rectangles show the region of interest. Both specimens have the Ti17 side on top and the Ti64 side at the bottom. To compare the strain evolution of ground-welded-1 and ground-welded-2 tensile specimens, the maximum macroscopic engineering strain on the horizontal axes of the spatio temporal graphs (Figs.8b, 8e, 8g and 8j) and the maximum local ϵ_{PP} strain on the colour bar of Figs.8a and 8f have been set to match the maximum values reached by the ground-welded-1 tensile specimen.

Failure at Ti64 PM The ground-welded-1 tensile specimen showed a maximum macroscopic engineering strain of 0.10 and a maximum local ϵ_{PP} strain of 0.34 exhibiting a slight stress drop and necking. Conversely, the ground-welded-2 tensile specimen showed a maximum macroscopic engineering strain of 0.05, a maximum local ϵ_{PP} strain of 0.11 and failed at the UTS (see Section 3.3). The heterogeneity of the ϵ_{PP} maps increases with increasing macroscopic strain for both specimens. Localization was observed at approximately $P = -7.5$ mm. Local strain was slightly greater over a region extending from the Ti64 PM to the Ti17 TMAZ (see Figs.8a 8f). The spatio-temporal graph of $\dot{\epsilon}_{PP}^{\text{norm}}$ for the ground-welded-1 tensile specimen highlights an early plastic activity in the vicinity of the WCZ at both TMAZs that gradually shifted to the Ti64 PM, leading to final rupture (see Fig.8c). This early plastic in the vicinity of the WCZ has already been observed for a similar Ti624Z LFW joints and was attributed to the presence of residual stresses by García and Morgeneyer [22] but here, it could also be linked to the low hardness of the weak Ti17 TMAZ.

Identification of the mechanically weak zone: Failure at Ti17 TMAZ The evolution of ϵ_{PP} and $\dot{\epsilon}_{PP}^{\text{norm}}$ for both tensile specimens is similar until map 7 and a macroscopic engineering strain of 0.05. It is interesting to note that, at the latest stages of deformation, the ϵ_{PP} and $\dot{\epsilon}_{PP}^{\text{norm}}$ maps of the ground-welded-1 tensile specimen exhibited similar gradients. This means that the maximum $\dot{\epsilon}_{PP}^{\text{norm}}$ occurred at the location of the maximum ϵ_{PP} , highlighting a continuous and steady evolution of strain, which is consistent with the smooth drop of macroscopic stress and necking. The behaviour of the ground-welded-2 tensile specimen at the final stages of deformation is strikingly different. Failure occurred at the Ti17 TMAZ and it was preceded by an abrupt jump of the $\dot{\epsilon}_{PP}^{\text{norm}}$ maximum from the Ti64 PM in map 7 to the Ti17 TMAZ in map 8 (see Figs.8h and 8i). Failure at Ti17 TMAZ is startling, since ϵ_{PP} reaches a maximum value of 0.11 at the Ti64 PM, which is substantially higher than the 0.06 reached at the Ti17 TMAZ. This suggests that the underlying α depleted β grains of the Ti17 TMAZ require low levels of plastic deformation to reach failure, which may also explain

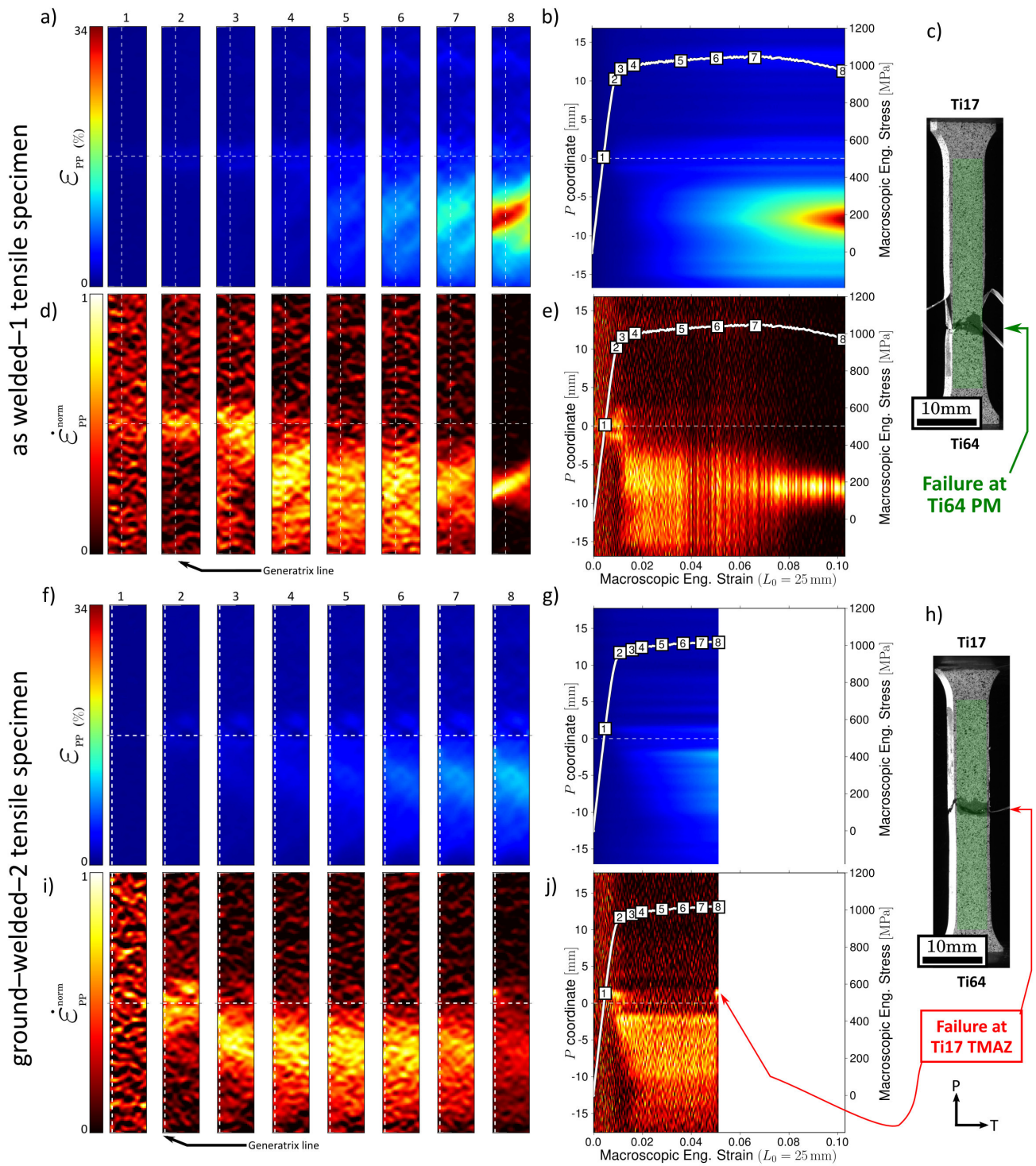


Figure 8: a,f) Cumulated strain maps; b,g) cumulated strain spatio-temporal graphs; d,i) normalized strain rate maps; e,j) normalized strain rate spatio-temporal graphs and c,h) *post-mortem* views of the tensile specimens in the load frame showing failure locations for the a-e) ground-welded-1 and f-j) ground-welded-2 tensile specimens.

both the sudden failure at UTS and the absence of necking for the ground-welded-2 tensile specimen. Given this abrupt failure, the Ti17 TMAZ is identified as a mechanically weak zone.

The $\dot{\epsilon}_{PP}^{\text{norm}}$ spatio temporal graphs have clearly revealed that some tensile specimens of the of the ground-welded LFW joint failed at the Ti17 TMAZ and some at the Ti64 PM. It seems that there was competition between the soft macro-zones of the Ti64 PM and the well-oriented α depleted β grains of the Ti17 TMAZ. The most remarkable fact is that failure never occurred at the WCZ, as was seen for the tensile specimens of the as welded LFW joints. The same set of welding parameters that failed to extrude the soft contaminants at the weld interface of the as welded LFW joint, favoured the development of an overmatching strength for the ground-as welded LFW joint.

3.3.2 Fracture mechanisms of the defect layer during tensile testing

The fracture surface of the as welded-1 tensile specimen is remarkably planar which is consistent with the fact that they failed in the elastic domain (see Fig.9a). Small equiaxed dimples surrounding the aforementioned elongated damage features can be observed in Fig.9b. This ductile rupture can be seen to a very limited occurrence. The fracture surface is mostly covered by features that suggest a pseudo brittle fracture, as seen in Fig.9c. These fracture mechanisms are unexpected for titanium alloys. A SEM/BSE observation of the fracture surface is shown in Fig.9d. Some grey contrast is observed. A light shade of grey predominates with some spots of a darker grey (see the spot surrounded by a white dashed line in Fig.9d). This contrast suggests that the chemical composition of the fracture surface was not homogeneous. To confirm this, EDX analyses have been performed on the fracture surface integrating the alloying elements of both PM's and copper. The chemical content in %wt over objects highlighting different grey levels are exhibited in the tables of Fig.9d. The blue and green points over the light and dark grey levels highlight chemical compositions that are comparable to Ti17 and Ti64, respectively. Contrary to expectations, substantial amounts of copper were measured even if this element was not contained in the nominal chemical composition of either of the parent materials. It should also be remembered that this specimen failed abruptly in the elastic domain. Self-evidently, bonding was fulfilled only in isolated spots and during monotonic loading, the weld interface was separated at the defect layer leading to a pseudo brittle fracture.

3.3.3 Fracture mechanisms under monotonic loading: ground-as welded tensile specimens

Failure at the Ti64 PM The ground-welded-1 tensile specimen failed at Ti64 PM and its fracture surface is shown in Fig.10. The observed dimples highlight ductile rupture and are comparable to

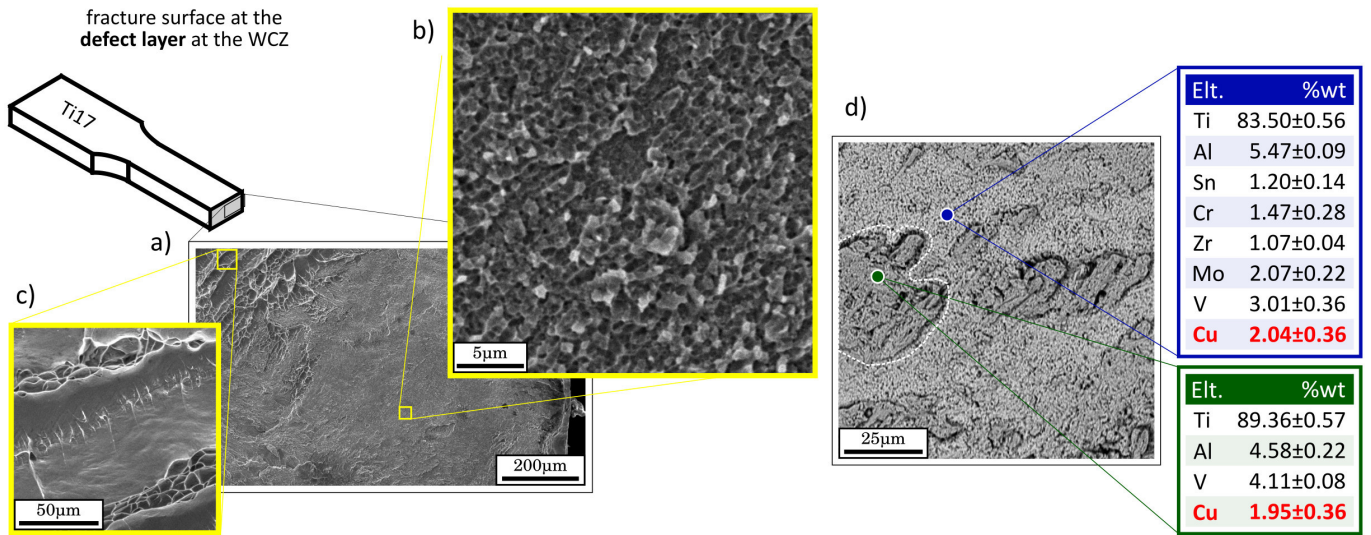


Figure 9: a) Fractographic observation of the as welded-1 tensile specimen showing mostly b) pseudo brittle fracture and some c) elongated damage features at the Ti17 TMAZ next to the defect layer. d) EDX point analysis of the fracture surface showing an approximation of the %wt. content of the PM alloying elements and Cu. Notice that some Cu is found despite the fact that this element did not belong to either of the parent materials' nominal chemical composition.

the dimples of Ti64 registered elsewhere [52]. The red arrows Fig.10a and 10b point to mesoscopic lines parallel to the RD direction of the PM billet. The presence of localized texture over bands parallel to the RD direction is well documented for Ti64 [3, 4, 5]. These so called macro-zones have been shown to be at the origin of the strain heterogeneity during micro tensile testing [4, 53] and to have an effect on impact toughness and the fracture behaviour [54]. It seems reasonable to conclude

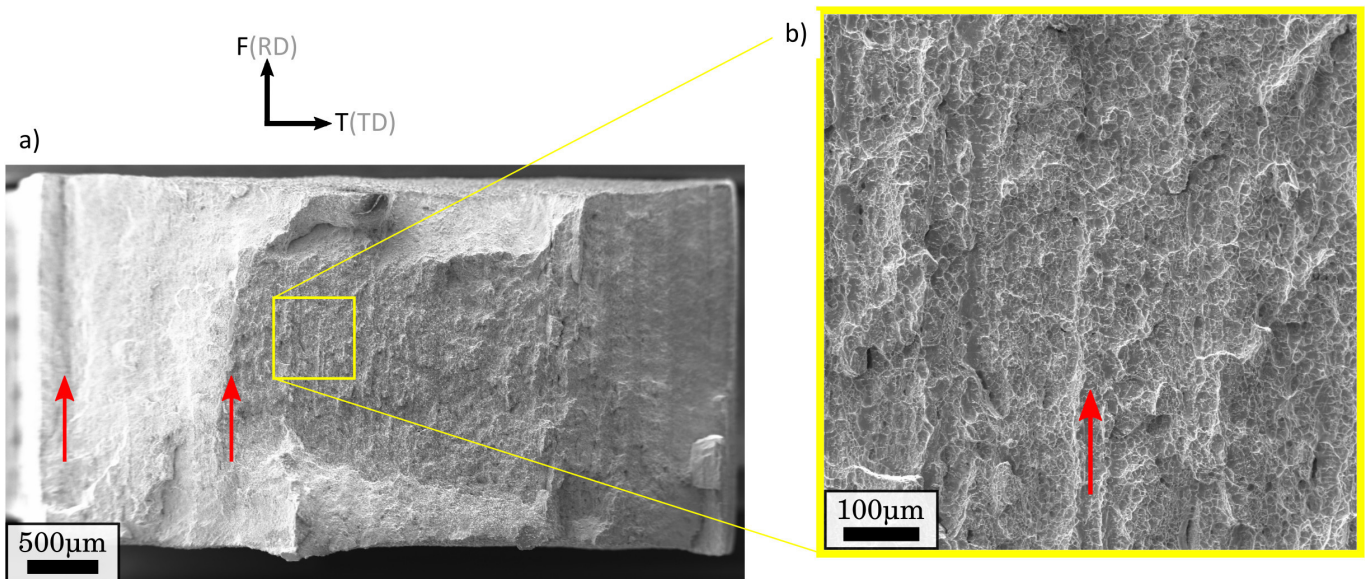


Figure 10: Fractographic observations showing ductile rupture at the Ti64 PM (at $P = -7.5$ mm) of the ground-welded-1 tensile specimen.

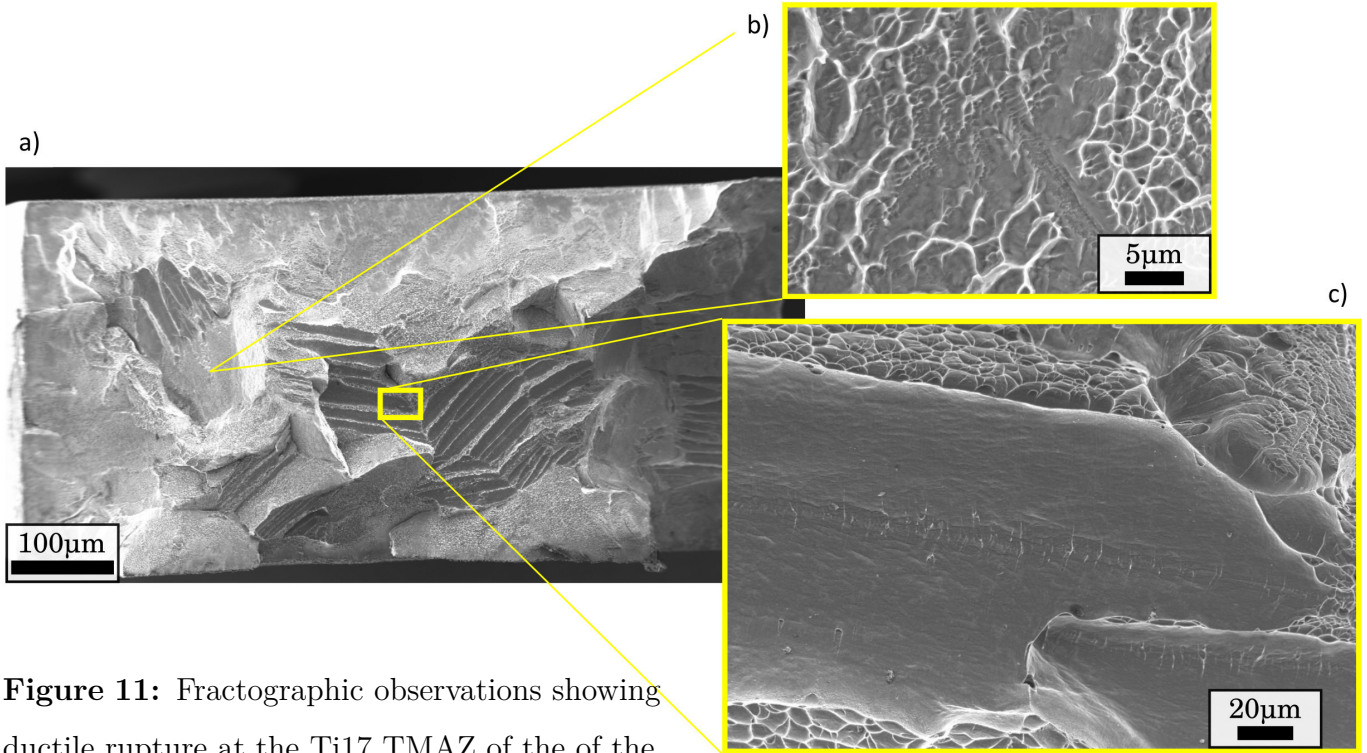


Figure 11: Fractographic observations showing ductile rupture at the Ti17 TMAZ of the of the ground-welded-2 tensile specimen.

that the alignments observed in the fracture surface are a consequence of potential underlying PM macro-zones.

Failure at the Ti17 TMAZ The ground-welded-2 tensile specimen abruptly failed at the Ti17 TMAZ (see Sections 3.3) and its fracture surface is shown in Fig.11. At first sight, it can be seen that clusters of elongated damage features (see Fig.11c) cover a substantial proportion of the fracture surface and are surrounded by classical titanium alloys dimples (see Fig.11b). These clusters of elongated damage features (see Fig.11) had been already seen in the fracture surface of another similar Ti17 LFW joint that also failed at the TMAZ [25]. The authors reported a macroscopic deformation of 2% on cross-weld tensile specimens for which failure occurred at the TMAZ. This suggests that local deformation at the TMAZ was greater. Moreover, Dalgaard et al. [26] measured a local deformation to failure of 9.28% for a similar Ti5553 LFW that also failed at the TMAZ. Considering these facts, it seems unlikely that the clusters of elongated damage features might be at the origin of a brittle fracture, as suggested by Li et al. [25]. These clusters of elongated damage features are further discussed in Section 3.5.

3.4 Fatigue test

The S–N curve for the fatigue specimens of the ground–as welded LFW joint is shown in the graph of Fig.12. For the sake of comparison, the S–N curve of the Ti17 PM is also shown. The fatigue specimens machined from the as welded and welded-heat treated LFW joints were not included in this graph since failure occurred at a very low number of cycles in some cases and at the first fatigue cycle for others. It should also be pointed out that their fracture surfaces (not shown here) were very similar to the fracture surface of the as welded–1 tensile specimen (see Fig.9). Closed and open symbols respectively represent the fatigue tests for which fracture occurred and those for which it did not (run out). For the target life of $N_f = 10^5$ cycles, the fatigue strength of the PM and cross-weld fatigue specimens respectively turned out to be 725 MPa and 450 MPa.

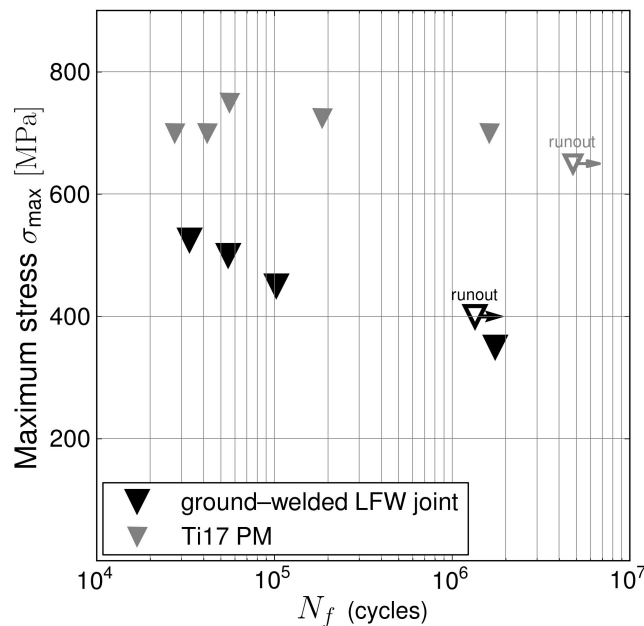


Figure 12: S–N curves for the fatigue specimens of the ground–as welded LFW joint (black triangles) and the Ti17 PM (grey triangles) ($R = 0.1$).

3.4.1 Fatigue crack initiation and propagation

Considering the results presented in previous Sections, it is possible to speculate about the potential location of the fatigue crack initiation on the welded structure of the fatigue specimens of the ground–welded LFW joint. First, it seems reasonable to postulate the Ti17 TMAZ and the Ti64 PM as candidates for fatigue crack initiation sites since they exhibited local minima on the microhardness profiles (see Section 3.2). Second, an early plastic activity in the vicinity of the WCZ was revealed by the $\varepsilon_{pp}^{\text{norm}}$ spatio-temporal graphs and was attributed to the presence of residual stresses (see Section 3.3.1). This location should be considered as a potential fatigue crack initiation site since

this was the scenario described for a LFW joint of a comparable titanium alloy previously studied by García and Morgeneyer [22]. The fatigue strength for both the Ti6242 PM and the similar Ti6242 LFW joint respectively turned to be 650 MPa and 625 MPa [22], which are higher than that of the ground-welded LFW joint.

Finally, in Section 3.3.1, the Ti17 TMAZ was identified as a weak zone since, during monotonic loading, localization abruptly shifted to this location and led to failure. Therefore, the Ti17 TMAZ weak zone is a potential fatigue crack initiation site and might exhibit a reduced fatigue strength.

Fig.13a shows a fractograph of a typical ground-welded fatigue specimen. Fatigue crack initiation occurred at the weak zone (Ti17 TMAZ). Figs.13c and 13d show respectively the primary and secondary fatigue crack initiation sites (see red arrows). It seems that fatigue crack initiated at the corner of the specimen potentially at the former α_{GB} layer of a β grain and propagated parallel to the green arrows in Fig.11a. A secondary fatigue crack also probably initiated at the former α_{GB} layer of a β grain at the specimen border and propagated parallel to the cyan arrows in Fig.11d. Final rupture exhibited elongated damage features (see Fig.13b) comparable to the ones seen in the fracture surface of the ground-welded-2 tensile specimen (see Fig.11).

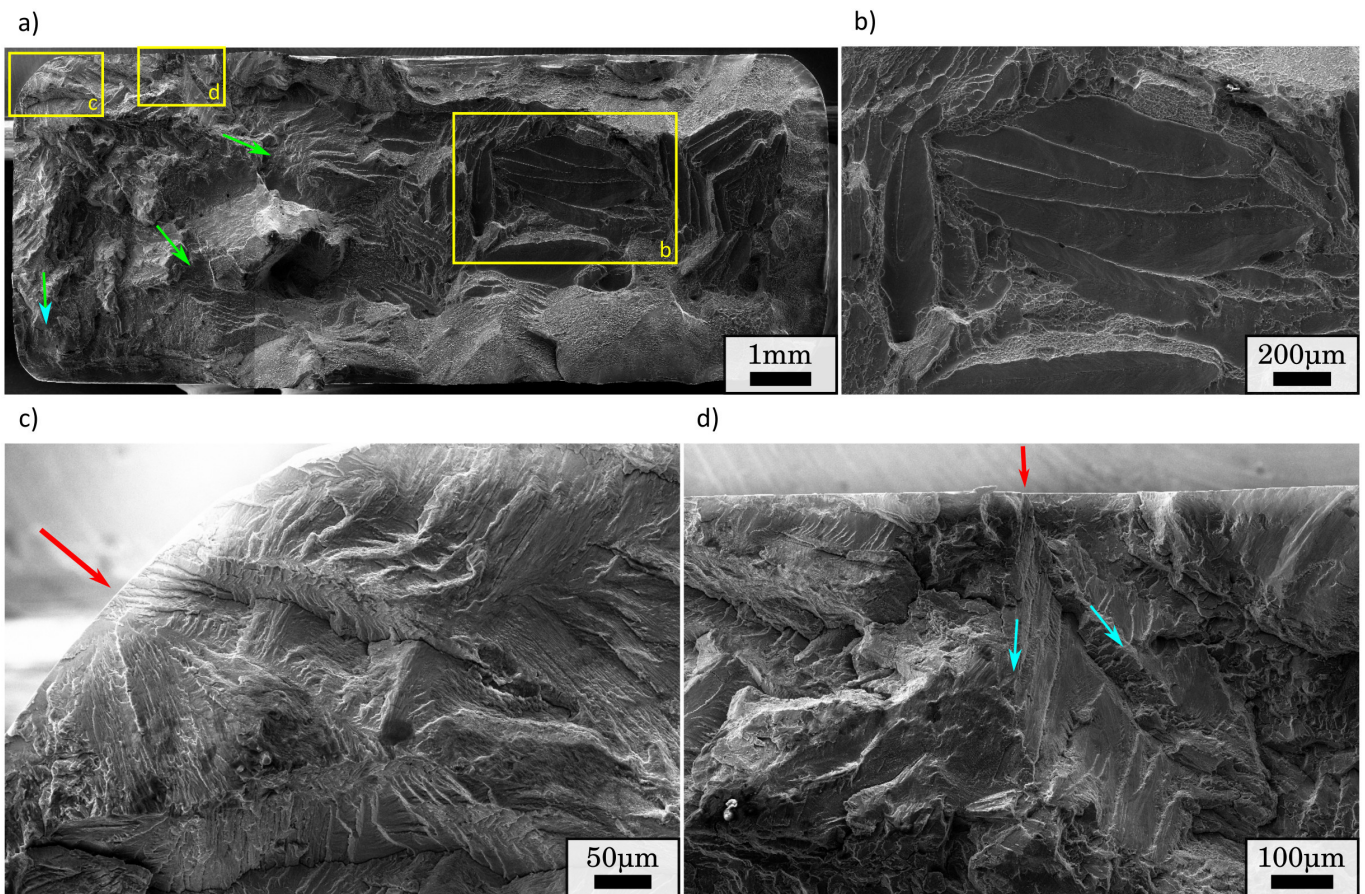


Figure 13: a) Fractograph of a typical fatigue specimen of the ground-welded LFW joint showing b) elongated dimples; c) primary and d) secondary fatigue crack initiation sites.

3.5 Fracture toughness

According to the *Blisks* specification, the disk made of Ti17 is meant to exhibit a high fracture toughness [1]. The aim of the fracture toughness experiments presented in this Section is threefold. First, to highlight the poor fracture toughness of the defect layer at the WCZ of the CT specimens machined from the as welded LFW joint. Second, to qualitatively compare the fracture toughness and fracture mechanisms of the CT specimens made of the Ti17 PM and those machined from the as welded and ground-welded LFW joints. Finally, to study the above mentioned potential cracking bifurcation from the WCZ to the Ti17 TMAZ of the ground-welded joint and its fracture mechanisms.

3.5.1 Fracture toughness results

Fig.14 shows the force - CMOD curves corresponding to the fracture toughness tests for the CT specimens of the Ti17 PM and the as welded and ground-welded LFW joints. The PM17 CT specimens showed a type-I force-displacement curve [46] with some plastic macroscopic deformation (see Fig.14a) whereas the cross-weld specimens showed an type-III force-displacement curve with a purely elastic macroscopic deformation (see Fig.14b and 14c).

According to the ASTM E1820-08 [46] standard, an extension of the machined crack must be fulfilled by a force-controlled cyclic loading to assure the reproducibility of results. The propagation of the fatigue pre-crack must be perpendicular to the load direction and its length should be controlled by optic observations at both sides of the CT specimen. Furthermore, for a proper computation of fracture toughness, the material of the CT specimens should be homogeneous. This adds difficulties in terms of machining and of fatigue pre-cracking the CT specimens. Although the thickness of the WCZ is in the order of hundreds of microns, the notches were machined and centred with respect to the WCZ with very good precision. However, fatigue pre-cracking was cumbersome for three reasons. First, the heterogeneous behaviour of the cross-weld CT specimens can provoke a bifurcation of the fatigue pre-cracking, namely towards the mechanically weak zones. Second, though the lateral observation of the fatigue pre-crack propagation assured the required fatigue crack length, *post-mortem* observations revealed that pre-cracks were much longer at the centre of the notch. Third, the CT specimens of the as welded LFW joint abruptly failed during pre-cracking, as a consequence of the poor mechanical properties of the defect layer. Due to these reasons, some specimens were tested with fatigue pre-cracks and some were tested without the fatigue crack extension. Although some of the results were not obtained in accordance to the standard requirements, they gave insight concerning the fracture mechanisms of the mechanically weak zone.

Considering the poor fracture toughness of the as welded LFW joint due to the presence of

the defect layer, the as welded-2 and the ground-welded-2 CT specimens were tested without pre-cracking to compute measurements of fracture toughness under comparable conditions. A total of 1.5×10^6 cycles were necessary to achieve a pre-crack extension of 0.9 mm on the sides of the ground-welded-1 CT specimen but *post-mortem* observations revealed that pre-crack extension at the centre was 2.9 mm. Thus, these tests were not in accordance to the standard requirements. The defect layer at WCZ of the as welded-1 CT specimen led a to pseudo brittle fracture during pre-cracking (not shown here). Nevertheless, their resulting fracture toughness computations are used here to perform a comparison. Detailed information about each test is given in Table 3.

The mean stress intensity factor computed using the Ti17-1 and Ti17-2 CT specimens trials turned out to be $K_{IC} = 99.0 \text{ MPa}\sqrt{\text{m}}$. Fracture toughness computations turned out to be $K_Q =$

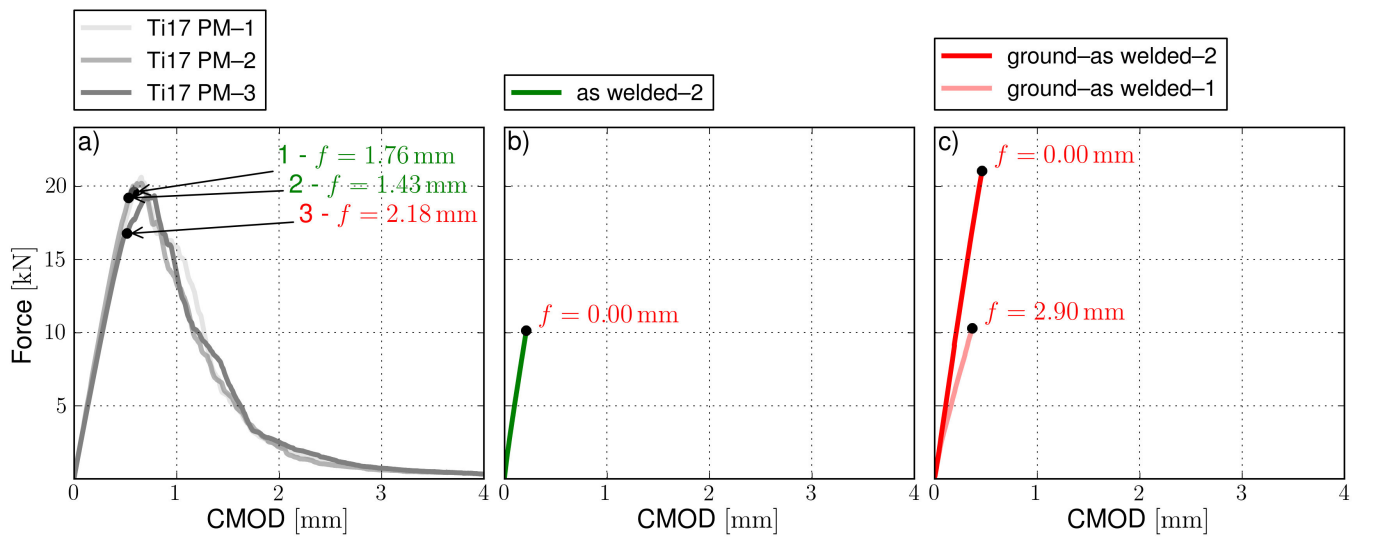


Figure 14: Force-CMOD curves for CT specimens of a) PM; b) as welded and c) ground-as welded LFW joints.

Table 3: Overview of fracture toughness experiment results for the CT specimens of the Ti17 PM and the as welded and ground-welded LFW joints. The validity of the test is determined following the [46] standard.

Specimen	K_i	($\text{MPa}\sqrt{\text{m}}$)	Pre-crack (mm)	Test	Observations
Ti 17-1	K_{IC}	102.1	1.76	Valid	–
Ti 17-2	K_{IC}	95.9	1.43	Valid	–
Ti 17-3	K_Q	92.3	2.18	Not valid	Excessive pre-crack.
as welded-1	K_Q	–	–	Not valid	Failure at defect layer during pre-cracking.
as welded-2	K_Q	45.7	0.00	Not valid	No pre-crack.
ground-welded-1	K_Q	62.6	2.90	Not valid	Excessive pre-crack.
ground-welded-2	K_Q	88.7	0.00	Not valid	No pre-crack.

45.7 MPa \sqrt{m} for the non pre-cracked as welded-2 CT specimen, $K_Q = 62.6$ MPa \sqrt{m} for the non pre-cracked ground-welded-1 CT specimen and $K_Q = 88.7$ MPa \sqrt{m} for the pre-cracked ground-welded-2 CT specimen. This shows that the grinding prior to welding substantially improved the fracture toughness of the welds. However, toughness of the improved welds was still reduced compared to that of the parent material.

3.5.2 Damage mechanisms of fracture toughness specimens

Fig.15a shows a fractograph of the ground-welded-2 CT specimen. The fracture surface is completely populated with elongated and flat dimples. These damage features were not observed in the parent material. Dimples appeared in clusters contained in regions that convey the shape prior β grains.

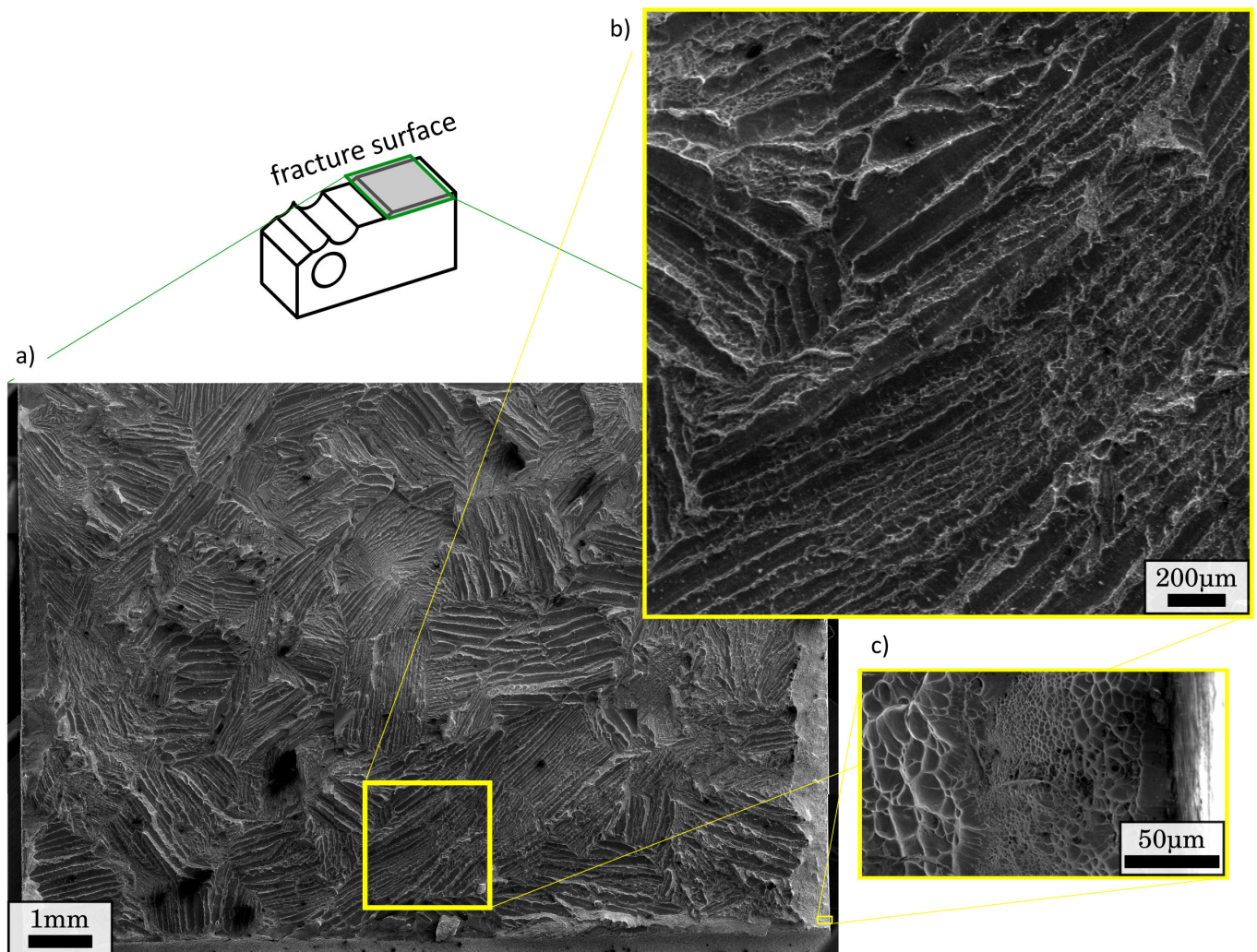


Figure 15: Fractograph of the ground-welded-2 CT specimen showing elongated damage features, close to the notch.

Failure occurred at Ti17 TMAZ during monotonic loading, cyclic loading and fracture toughness testing (see Sections 3.3.2, 3.4.1 and 3.5). In all fracture surfaces, clusters of elongated damage

features were observed. To better understand the origin of these clusters of elongated fracture surfaces, a *post-mortem* analysis of the microstructure next to the fracture surface of the ground-welded-2 CT specimen is presented in this Section.

After performing the fractographic analysis, the Ti17 side of the ground-welded-2 CT specimen was cut in halves parallel to a FP plane, as shown in the schematic view of Fig.16a. As a reminder, this specimen failed at the α depleted Ti17 TMAZ and the fracture surface exhibited showed exclusively clusters of elongated fractures features. These two points can easily be recognized in Fig.16b, since the chemical contrast observed in the SEM/BSE observation hints to the α depletion of the mechanically weak zone and the toughness of the fracture surface recalls the morphology of the elongated damage features. For instance, the yellow dashed line of Fig.16c highlights some relief on the fracture surface that is similar to the elongated damage features observed in the fractographic analysis of this specimen (see Fig.16). It seems that the damage feature was cut on a plane perpendicular to its main axis.

In the CMOD-F curve of this specimen (see Fig.14), it was observed that the crack propagated abruptly at a maximum stress during elastic loading. It could be imagined that these damage features were at the origin of a brittle fracture, as suggested by Li et al. [25]. To verify this, the entire weak zone was inspected to identify potential nucleation of the elongated damage features. Indeed, in Figs.16c, 16d, 16f and 16g, rhombus-shaped voids were observed. This is very interesting because it shows that the elongated features appeared as a result of a nucleation and growth process as a ductile mechanism. However, it should be noted that the nucleation and growth of these elongated features required very low deformation and associated energy, as observed in the CMOD-F curve for this specimen.

A question about the underlying microstructural features at the origin of these elongated damage features may arise. The specimen was etched after performing the SEM/BSE observation of Fig.16c. Thereafter, the SEM observation of the surroundings of the elongated damage features nucleation was performed (see Fig.16d). Notice that although the microstructure at the Ti17 TMAZ consisted in α depleted β grains, the roughness of the etched specimen recalls the former α_{WI}^p plates inside the β grain of the PM. This suggests that, despite the α depletion, the etching interacted with the former α_{WI}^p plates and generated the specimen roughness. To confirm this, a SEM/BSE observation of the Ti17 PM at the same level of magnification is shown in Fig.16e. The characteristic angles between the α_{WI}^p plates at the core of the β grain seen in Fig.16e are recognized in the relief patterns of Fig.16f.

It should be noted that not only did the elongated damage features nucleate parallel to former α_{WI}^p plates, but also they seem to be contained in a deformation line that sheared the former α_{WI}^p

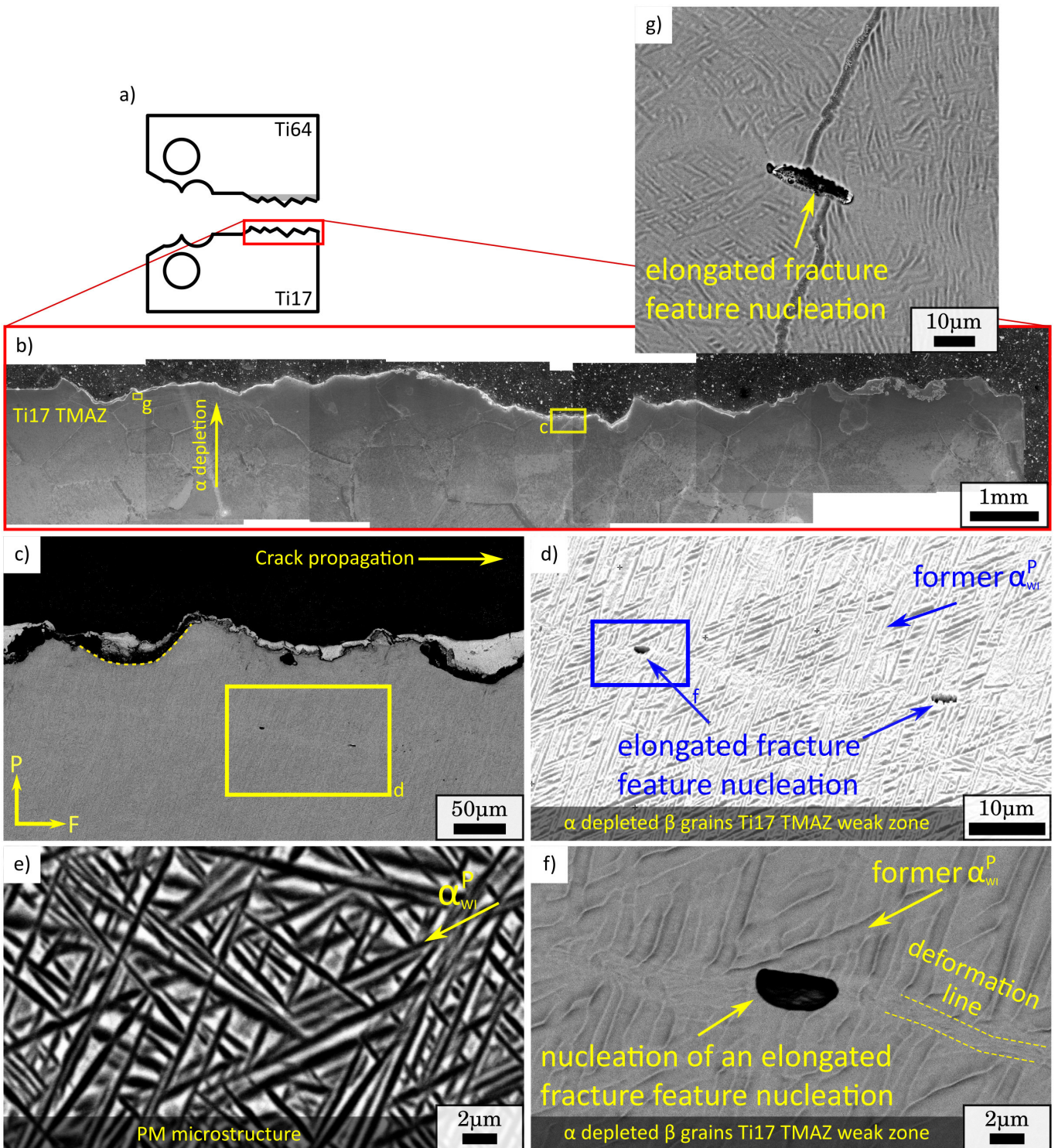


Figure 16: Fractographic analysis of the ground-welded-2 CT specimen showing : a) a schematic view of the *port-mortem* cut specimen to study damage mechanisms and the underlying microstructure ; b) a SEM/BSE observation of the crack highlighting the underlying microstructure ; observations of nucleation of elongated damage features a) close to the fracture surface and d) after etching ; SEM/BSE observations of the e) α_{WI}^P plates inside a β grain of the PM ; f) the nucleation of an elongated damage feature over a deformation line parallel to a former α_{WI}^P plate and g) zoom on a void indicated in 16b.

plates. Notice the deformation line highlighted by the yellow dashed lines in Fig.16f. Similarly, in Fig.16g, the elongated damage features seem to have nucleated in a former α_{WGB} colony. This suggests that this deformation process involves a crystallographic orientation relationship, as the typical transformation between α and β first studied by Burgers [55].

Fig.17a shows SEM/BSE observation of Fig.16g. To further the analysis, EBSD observations were carried out on the region highlighted by the yellow dashed rectangle of Fig.17a. The EBSD image quality map and the phase map are respectively shown in Figs.17b and 17c. Notice that the crystal lattice in this region is mostly β (see Fig.17), which is consistent with the EBSD observation of the TMAZ performed by Ballat-Durand et al. [15] and Dalgaard et al. [26]. The grain boundary is severely sheared (see Fig.17a) and the image quality is lower at the deformation line (see Fig.17b). These findings are consistent with high levels of local deformation, which also explains the nucleation of damage features. Earlier in this Section, it was suggested that these deformation lines seem to follow crystallographic orientations. During the deformation of β titanium alloys at room temperature studied by Karasevskaya et al. [56], Aeby-Gautier et al. [57], Duerig et al. [58] and Menon et al. [59], the formation of a stress induced orthorhombic α'' martensite was observed. Duerig et al. [58] and [59] observed that its formation occurred respecting crystallographic orientation relationships, although they do not agree about which one was activated. Furthermore, Karasevskaya et al. [56] observed the formation of fine precipitations of α'' along comparable strain lines. It seems very likely that the strain line shown in Fig.17a is the consequence of the formation of strain induced orthorhombic α'' martensite but nevertheless, the results provided here are not conclusive.

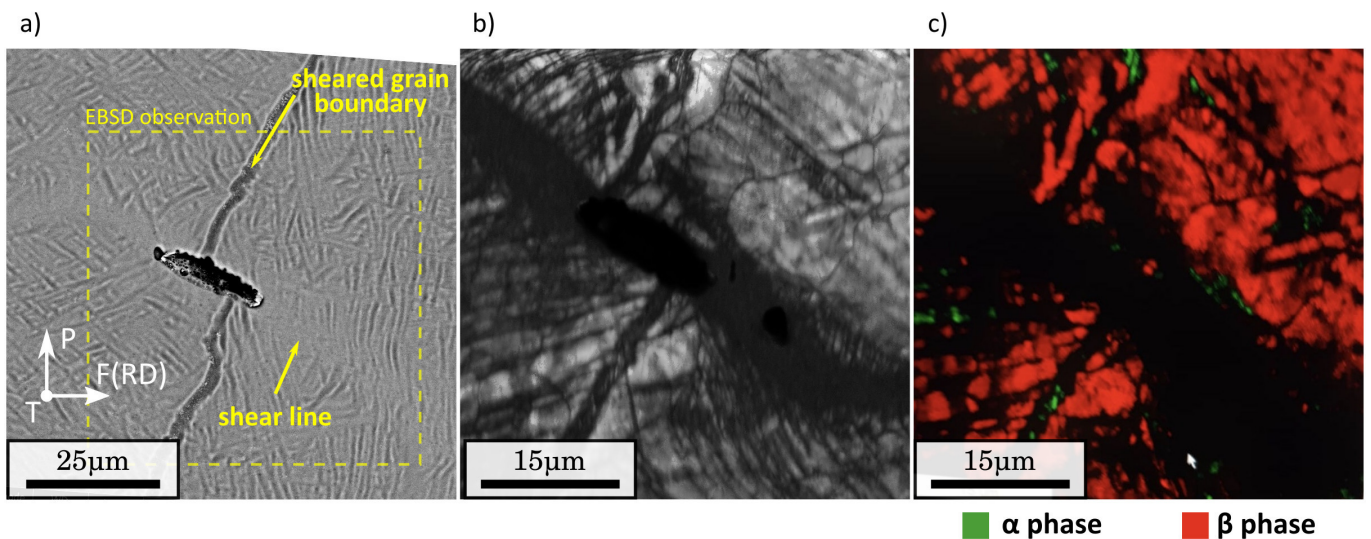


Figure 17: a) SEM/BSE observation of Fig.16g showing a damage feature, a strain line, a sheared grain boundary and the area to be analysed by EBSD observations; b) EBSD quality image mapping and c) phase map showing the α phase in green and the β in red.

4 Discussion

4.1 Defect layer, welding parameters and surface preparation

In this work, three joints were produced using the same set of welding parameters. The first joint was welded having the PM's blocks in the as machined state after electrical discharge machining (as welded LFW joint), the second was welded after electrical discharge machining and was post-weld heat treated (welded-head treated LFW joint), and the third was ground prior to welding using a 1200 grit SiC paper for 2 min (ground-welded LFW joint). A defect layer probably formed by oxides was observed in the as welded LFW joint and contained the soft contaminants in the weld interface. Interestingly, this defect was not observed in the ground-welded LFW joint. The defect layer exhibited an undesirable pseudo brittle fracture in the elastic domain during monotonic loading, cyclic loading and fracture toughness tests. The fractographic analysis of the tensile specimen of the as welded LFW joint clearly revealed the separation of the WCZ as a consequence of very poor bonding (see Section 3.3.2). Conversely, failure never occurred at the WCZ for the tensile specimens of the ground-welded LFW joint. It could be argued that the power input provided to the ground-welded LFW joint was enough to favour the development of overmatching strength but not enough to properly extrude the soft contaminants at the weld interface of the as welded LFW joint.

It could be argued that the soft contaminants would not be an issue for widely used industrial machining techniques, such as water jet machining. However, the presence and effective extrusion of contaminants in general has already been largely discussed in the literature. For instance, some very interesting numerical approaches have been proposed for the optimization of welding parameters. They consist in verifying if a certain set of welding parameters accomplishes the effective extrusion of tracking points at the weld interface by the end numerical simulations of the welding process [36, 37, 38, 39]. Their limitations seem nonetheless to be that the tracking points bear the physical properties of the PM, instead of bearing those of the contaminants. Performing numerical simulations taking into account the nature of contaminants seems cumbersome since the nature of contaminants and subsequently their behaviour are *a priori* unknown. Furthermore, considering the 5 μm thickness of the defect layer, the optimization of welding parameters through a numerical approach by considering the nature of contaminants seems rather not to be feasible.

The surface preparation prior to LFW has been approached differently by researchers published in the scientific literature. A literature review concerning the surface preparation techniques is shown in the chart of Fig.18. Four classes have been identified: welding after alcohol/acetone bath, welding after grinding, welding in the as machined state and welding without specifying the surface

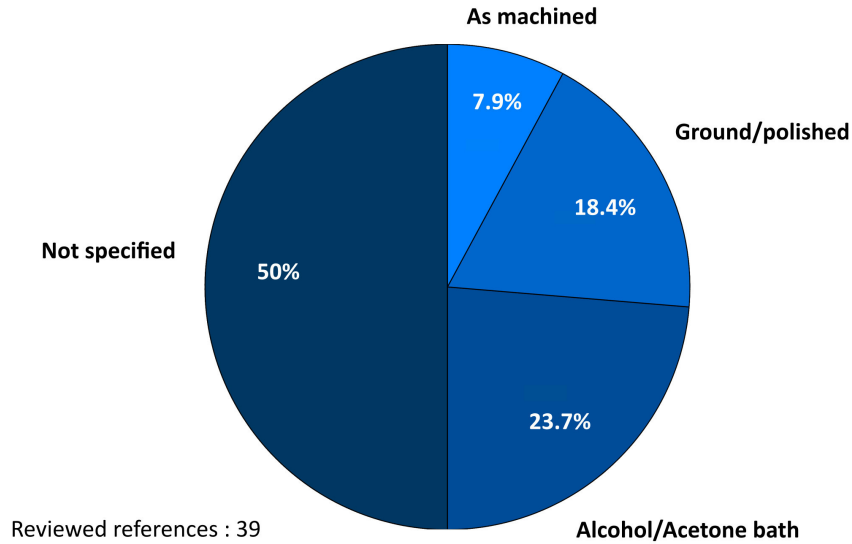


Figure 18: Literature review concerning the surface preparation for linear friction welding.

preparation. About 42 % of the population adopted a surface preparation technique and only 7.9 % of them have specified welding in the as machined state. This is rather puzzling since LFW is reputed to be a self-cleaning process. In the mechanical characterization of the dissimilar linear friction welding between a SiC particle reinforced aluminium composite and a monolithic aluminium conducted by Rotundo et al. [40], the authors claimed :

“Since the surface oxide layer originating from the electrical discharge machining wire cutting was expected to be expelled during the LFW, the specimens were not submitted to any further machining prior to welding [...].”

Yet, the fractographs for both tensile and fatigue specimens in their study exhibited pseudo-brittle features very similar to the ones shown in Fig.9 with the difference that some plastic macroscopic deformation was observed. Interestingly, fatigue cracks seem to have initiated at the TMAZ but at final rupture, a de-cohesion of the WCZ appears to have occurred due to the presence of a potential oxide layer.

Only 18.4 % of the researchers ground the surfaces to be welded prior to LFW. The addition of a 2 min grinding operation prior to welding is a rather simple and economical practice. Its implementation should seriously be considered since not only does it seem to bolster the self-cleaning property of LFW but it also leads to LFW joints with dramatically enhanced mechanical properties (see Fig.7). Finally, half of the researchers did not specify the surface preparation technique. This, in junction with the diversity of the adopted surface preparation techniques, could be interpreted as a symptom of one issue amongst others, that has prevented LFW of becoming a more popular technique: The lack of a standard. The creation of a standard for LFW should definitely include a

paragraph concerning the surface preparation. Despite more experimental research being necessary to sustain this, it is advised to perform a 2 min grinding operation with a 1200 grit SiC paper followed by an acetone bath, a few minutes before LFW.

4.2 Failure at the Ti17 TMAZ of the ground–welded LFW joint

The specification for the fabrication of Blisks states that the disk should exhibit high tensile strength and resistance under low cycle fatigue crack, whilst the blades should show creep resistance and high cycle fatigue [1]. Thus, disks can be made of Ti17 (or Ti6246) and the blades of Ti64 (or Ti6242). Some of tensile specimens failed far from the WCZ at the Ti64 side (see Section 3.3.1). This is desirable since it implies that both Ti17 and the WCZ have higher strengths. Nevertheless, some of the tensile specimens failed abruptly at the Ti17 TMAZ with a significant reduction in ductility and without necking.

For a similar Ti6242 LFW joint, an early plastic activity in the vicinity of the WCZ that later shifted to the PM was highlighted using normalized strain rate spatio-temporal graphs [22]. This phenomenon was attributed to the presence of residual stresses at this location and was at the origin of fatigue crack initiation. As for the tensile specimens studied here, regardless of the location of the final failure on the welded structure, the same early plastic activity at the Ti64 TMAZ and the same shift to the Ti64 PM were observed (see Fig.8). This hints at the presence of residual stresses at this location. Interestingly, for the cross-weld fatigue specimens studied here, fatigue crack always initiated at the Ti17 TMAZ. This is particularly astonishing because it seems that, in terms of cyclic behaviour, the microstructure at the Ti17 TMAZ is a bigger threat to the integrity of the welded structure than the residual stresses at the Ti64 TMAZ.

The blades of the disk are meant to resist high cycle fatigue. Therefore, for a fatigue life of 10^5 cycles, it may reasonably be stated that fatigue crack initiation occurring at the Ti17 TMAZ is acceptable. In spite of that, the fatigue strength of the cross-weld fatigue specimens (450 MPa) is much lower than the fatigue strength of both PM's (750 MPa). Moreover, for the fracture toughness tests of Section 3.5, the values of fracture toughness were particularly low and exhibited a pseudo-brittle fracture at the Ti17 TMAZ. Considering the behaviour of cross-weld specimens during fracture toughness tests and monotonic and cyclic loadings, it seems clear that the Ti17 TMAZ is an important threat to the integrity of the welded structure.

Thermal treatments are largely used after friction welding [60]. For instance, the similar Ti5553 LFW joint studied by Dalgaard et al. [26] exhibited failure at the Ti17 TMAZ but after the application of a solution treatment and ageing thermal treatment, Wanjara et al. [27] showed that failure no

longer occurred at the former Ti17 TMAZ. Similarly, Ballat-Durand et al. [15] proposed a standard solution treatment and ageing heat treatment that seems to restore the PM microstructure of a similar Ti17 LFW joint. García et al. [61] compared the monotonic and cyclic behaviour of similar Ti17 LFW joints in the as welded state and in the heat treated state, as proposed by Ballat-Durand et al. [15]. This heat treatment successfully favoured the α precipitation in the WCZ and TMAZ and led to mechanical properties that were comparable to the similar Ti17 LFW joint [61]. However, the application of this thermal treatment for Blisks does not seem feasible due to the large size of the component and how this treatment could affect texture in the core of the Blisks. Instead, the application of an annealing heat treatment would seem to be enough to favour the α precipitation in the TMAZ and the WCZ without affecting the microstructure of the rest of the components.

5 Conclusions

The effect of microstructure, particularly in terms of soft contaminants and alpha precipitate depletion, of three dissimilar Ti17-Ti64 linear friction welded joints on the strength, fatigue strength and fracture toughness was studied. The mechanical behaviour in terms of tensile strength, fatigue strength and fracture toughness of the microstructure of three dissimilar Ti17-Ti64 LFW joints has been studied. The first was joined in the as machined state after electrical discharge machining (as welded LFW joint), the second was welded after electrical discharge machining and was post-weld heat treated (welded-heat treated LFW joint), and the third was ground prior to welding using a 1200 grit SiC paper for 2 min (ground-welded LFW joint) to eliminate soft contaminants in the surfaces to be welded. Results led to the following conclusions:

- The microstructure of the WCZ showed 10 μm diameter α depleted β grains in the Ti17 side and an acicular entangled α' martensite with a Widmanstätten morphology in the Ti64 side. The β microstructure of Ti17 PM suffered a depletion of the α phase in the WCZ and the TMAZ that led to the creation of mechanically weak zones at the Ti17 TMAZ.
- The as welded LFW joint presented a defect layer rich in Ti, Al and O of possibly oxides that led to an undesirable pseudo-brittle rupture in the elastic domain during tensile testing, fatigue testing and fracture toughness testing. This defect layer contained Cu and Zn contamination caused by the brass wire during electrical discharge machining of the PM's blocks prior to welding.
- The tensile specimens of the ground-welded LFW joint presented a mean UTS of 1050 MPa and considerable scatter in macroscopic strain to failure since two failure scenarios were ob-

served. No defect layer was observed. Some tensile specimens failed at the Ti64 PM presenting a macroscopic strain to failure of 0.10 and ductile rupture. Some tensile specimens failed, however, at the Ti17 TMAZ exhibiting a macroscopic strain to failure of 0.05 and a failure at elongated dimples at the weak zone (Ti17 TMAZ).

- Normalized strain rate spatio-temporal graphs showed an early plastic activity in the vicinity of the WCZ that later shifted to the Ti64 PM for all the tensile specimens of the ground-welded LFW joint. In spite of this, some tensile specimens failed at Ti17 TMAZ.
- For the target fatigue life of 10^5 cycles, the fatigue strength of the fatigue specimens of the ground-welded LFW joint was 450 MPa. During cyclic loading, fatigue crack initiated at the former α_{GB} precipitates at the β grains of the Ti17 TMAZ).
- The CT specimens of the as welded LFW joint showed very low fracture toughness failing at the maximum load exhibiting a pseudo-brittle damage features at the defect layer. The specimens of the ground-welded LFW joint showed higher fracture toughness but still lower than the PM CT specimens highlighting a fracture surface completely populated by elongated damage features occurring in deformation lines parallel to the former α_{WI}^p plates, at the α depleted β grains of the Ti17 TMAZ.
- The Ti17 TMAZ was identified as a mechanically weak zone since failure occurred during monotonic loading, cyclic loading and fracture toughness testing.
- The threat to the integrity of the welded structure given by the defect layer was not solved by the application of the post weld heat treatment. Conversely, the applied surface preparation for LFW led to more desirable mechanical properties in terms of tensile strength, fatigue strength and fracture toughness. The self-cleaning mechanism of LFW is reliable to some extent.

6 Acknowledgements

The authors wish to thank *UTC*, *CEMEF*, *Mines-ParisTech* and Airbus Central R&T for the valuable discussions. ACB is thanked for providing the welds for this study. Yvon Millet at Timet is acknowledged for his insight in microstructure analysis. Anne-Françoise Gourgues-Lorenzon at *Centre des Matériaux* is kindly thanked for the discussions about rupture mechanisms. Jérôme Delfosse (SAFRAN, France), Achilles Vairis (Technological Education Institute of Crete), Anthony McAndrews (TWI, UK) and Bertrand Flipo (TWI, UK) are gratefully acknowledged for the kind discussions on the self-cleaning mechanism of LFW. The authors acknowledge the financial support from

the French National Research Agency (ANR) and FRAE through OPTIMUM ANR-14-CE27-0017 project.

Data availability

The raw/processed data required to reproduce these findings cannot be shared at this time due to technical or time limitations.

Appendix A Normalized strain rate: Strain increment/strain uncertainty ratio

Eq.1 introduces the expression of the normalised strain rate, which is used in Figs.8d and 8e to highlight an early plastic activity in the surroundings of the WCZ. Since the strain rate is normalized with respect to its maximum value for each level of macroscopic engineering strain, the notion of the strength of strain rate signal is lost. In such a case, the strain increment used in the computation of the normalised strain rate (see Eq.1) may turn out to be comparable to the strain uncertainty. To make sure this is not the case, the ratio between the strain increment and the strain uncertainty is plotted in the graph of Fig.19. The macroscopic engineering strain and stress are respectively plotted in the horizontal and secondary vertical axis. The primary vertical axis represents the strain increment/strain uncertainty ratio. The tensile curve of a specimen that failed at the Ti64 PM is

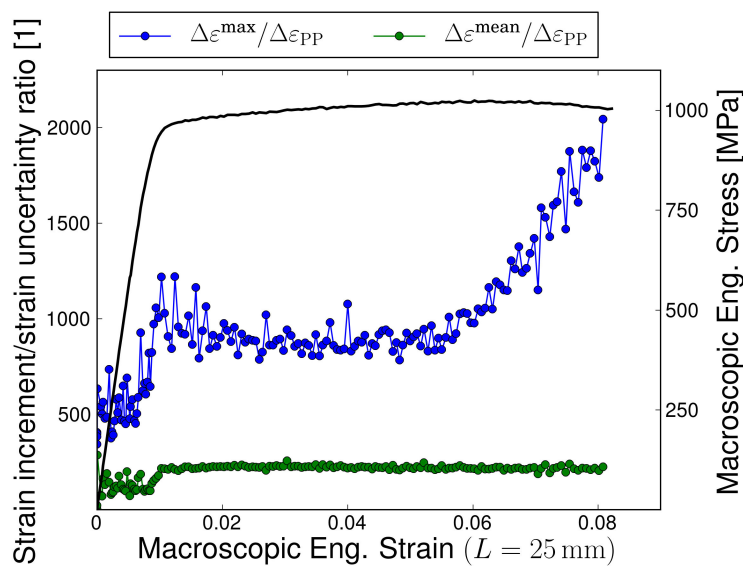


Figure 19: Strain increment/strain uncertainty evolution and comparison with macroscopic tensile curve for a tensile specimen that failed at the Ti64 PM.

plotted in black. The average strain increment and the maximum strain increment in the entire observed field were computed for each level of macroscopic engineering. Their evolution with respect to the macroscopic engineering strain are respectively plotted in green and in blue. It should be considered that with this computation, the location of the maximum strain increment in the region of interest might change as the macroscopic engineering strain increases. The strain uncertainty was experimentally measured in Section 2.4 and turned to be $\Delta\varepsilon_{PP} = 0.0002$.

Notice that from the elastic domain of the macroscopic engineering deformation, the mean strain increment/strain uncertainty ratio is in the order of $1e2$ and continues to increase up to $2.5e2$ (green curve in Fig.19). Similarly, the maximum strain increment/strain uncertainty ratio is in the order of $5e3$ and continues to increase up to $2e4$ (blue curve in Fig.19). This confirms that the strain increment signal is considerably strong. It should also be noticed that, as the macroscopic engineering strain enters in the plastic domain, an abrupt jump is observed in the strain increment/strain uncertainty ratio. This is consistent with the early plastic activity observed in the graphs of Figs.8d and 8e. Furthermore, as the macroscopic engineering stress reaches its maximum, an inflexion point is observed in the blue curve, which is consistent with strain localization at the Ti64 PM observed in Fig.8e.

References

- [1] Antonio M. Mateo García. Blisk fabrication by linear friction welding. In Ernesto Benini, editor, *Advances in Gas Turbine Technology*, chapter 18. IntechOpen, Rijeka, 2011. doi: 10.5772/21278. URL <https://doi.org/10.5772/21278>.
- [2] ME Nunn. Aero engine improvements through linear friction welding. In *1st International conference on innovation and integration in aerospace sciences*, pages 4–5. CEIA, Queen’s University Belfast Northern Ireland, UK, 2005.
- [3] K. Le Biavant, S. Pommier, and C. Prioul. Local texture and fatigue crack initiation in a ti-6al-4v titanium alloy. *Fatigue & Fracture of Engineering Materials & Structures*, 25(6):527–545, 2002. doi: 10.1046/j.1460-2695.2002.00480.x. URL <https://onlinelibrary.wiley.com/doi/abs/10.1046/j.1460-2695.2002.00480.x>.
- [4] McLean P. Echlin, Jean Charles Stinville, Victoria M. Miller, William C. Lenthe, and Tresa M. Pollock. Incipient slip and long range plastic strain localization in microtextured ti-6al-4v titanium. *Acta Materialia*, 114:164 – 175, 2016. ISSN 1359-6454. doi: <https://doi.org/10.1016/j.actamat.2016.04.014>.

- 1016/j.actamat.2016.04.057. URL <http://www.sciencedirect.com/science/article/pii/S1359645416303251>.
- [5] Matthew Kasemer, McLean P. Echlin, Jean Charles Stinville, Tresa M. Pollock, and Paul Dawson. On slip initiation in equiaxed α/β ti-6al-4v. *Acta Materialia*, 136:288 – 302, 2017. ISSN 1359-6454. doi: <https://doi.org/10.1016/j.actamat.2017.06.059>. URL <http://www.sciencedirect.com/science/article/pii/S1359645417305360>.
- [6] R.R. Boyer. An overview on the use of titanium in the aerospace industry. *Materials Science and Engineering:A*, 213(1):103 – 114, 1996. ISSN 0921-5093. doi: [https://doi.org/10.1016/0921-5093\(96\)10233-1](https://doi.org/10.1016/0921-5093(96)10233-1). URL <http://www.sciencedirect.com/science/article/pii/S0921509396102331>. International Symposium on Metallurgy and Technology of Titanium Alloys.
- [7] Ioannis Bantounas, Trevor C. Lindley, David Rugg, and David Dye. Effect of microtexture on fatigue cracking in ti6al4v. *Acta Materialia*, 55(16):5655 – 5665, 2007. ISSN 1359-6454. doi: <https://doi.org/10.1016/j.actamat.2007.06.034>. URL <http://www.sciencedirect.com/science/article/pii/S1359645407004338>.
- [8] Abkowitz Stanley. Heat treated titanium-aluminumvanadium alloy, September 29 1959. US Patent 2,906,654.
- [9] Gerhard Welsch, Rodney Boyer, and EW Collings. *Materials properties handbook: titanium alloys*. ASM international, 1993.
- [10] Gerd Lütjering and James Case Williams. *Titanium*, volume 2. Springer, 2003.
- [11] Srikumar Banerjee and Pradip Mukhopadhyay. *Phase transformations: examples from titanium and zirconium alloys*, volume 12. Elsevier, 2010.
- [12] GW Meetham. *The Development of Gas Turbines*. Springer, 1981.
- [13] J. Romero, M.M. Attallah, M. Preuss, M. Karadge, and S.E. Bray. Effect of the forging pressure on the microstructure and residual stress development in ti6al4v linear friction welds. *Acta Materialia*, 57(18):5582 – 5592, 2009. ISSN 1359-6454. doi: <https://doi.org/10.1016/j.actamat.2009.07.055>. URL <http://www.sciencedirect.com/science/article/pii/S135964540900490X>.
- [14] P. Frankel, M. Preuss, A. Steuwer, P. J. Withers, and S. Bray. Comparison of residual stresses in ti6al4v and ti6al2sn4zr2mo linear friction welds. *Materials Science and Technology*, 25(5):640–650, 2009. doi: [10.1179/174328408X332825](https://doi.org/10.1179/174328408X332825). URL <https://doi.org/10.1179/174328408X332825>.

- [15] Dorick Ballat-Durand, Salima Bouvier, Marion Risbet, and Wolfgang Pantleon. Multi-scale and multi-technic microstructure analysis of a linear friction weld of the metastable- β titanium alloy ti-5al-2sn-2zr-4mo-4cr (ti17) towards a new post-weld heat treatment. *Materials Characterization*, 144:661 – 670, 2018. ISSN 1044-5803. doi: <https://doi.org/10.1016/j.matchar.2018.08.013>. URL <http://www.sciencedirect.com/science/article/pii/S1044580318312671>.
- [16] Xinyu Wang, Wenya Li, Tiejun Ma, Xiawei Yang, and Achilles Vairis. Microstructural evolution and mechanical properties of a linear friction welded two-phase Ti-6.5Al-3.5Mo-1.5Zr-0.3Si titanium alloy joint. *Materials Science & Engineering:A*, 743:12 – 23, 2019. ISSN 0921-5093. doi: <https://doi.org/10.1016/j.msea.2018.11.059>. URL <http://www.sciencedirect.com/science/article/pii/S0921509318315855>.
- [17] W.A. Baeslack, T.F. Broderick, M. Juhas, and H.L. Fraser. Characterization of solid-phase welds between Ti-6Al-2Sn-4Zr-2Mo-0.1Si and Ti-13.5Al-21.6Nb titanium aluminide. *Materials Characterization*, 33(4):357 – 367, 1994. ISSN 1044-5803. doi: [https://doi.org/10.1016/1044-5803\(94\)90140-6](https://doi.org/10.1016/1044-5803(94)90140-6). URL <http://www.sciencedirect.com/science/article/pii/1044580394901406>.
- [18] E Dalgaard, P Wanjara, J Gholipour, and J J Jonas. Evolution of microstructure, microtexture and mechanical properties of linear friction welded imi 834. *Canadian Metallurgical Quarterly*, 51(3):269–276, 2012. doi: 10.1179/1879139512Y.0000000014. URL <https://doi.org/10.1179/1879139512Y.0000000014>.
- [19] W. Ritcher. Herbeifuehrung einer haftverbindung zwischen plaettchen aus werkzeugstahl und deren traegern nach art einer schweissung oder loetung, 05 1929. URL https://www.lens.org/lens/patent/DE_476480_C.
- [20] A. I. Chudikov. Friction welding, 1956. Russian Patent, RU106270.
- [21] R Maurya and J Kauzlarich. Reciprocating friction bonding apparatus. *Patent nos. US3420428-A, DE1552871-A, CA844858-A*, 1969.
- [22] Juan Manuel García and Thilo F. Morgeneyer. Strength and fatigue strength of a similar Ti-6Al-2Sn-4Zr-2Mo-0.1Si linear friction welded joint. *Fatigue & Fracture of Engineering Materials & Structures*, 42(5):1100–1117, 2019. doi: 10.1111/ffe.12973. URL <https://onlinelibrary.wiley.com/doi/abs/10.1111/ffe.12973>.
- [23] Yingping Ji, Sujun Wu, and Dalong Zhao. Microstructure and mechanical properties of friction welding joints with dissimilar titanium alloys. *Metals*, 6(5), 2016. ISSN 2075-4701. doi: 10.3390/met6050108. URL <https://www.mdpi.com/2075-4701/6/5/108>.

- [24] Yajuan Ji, Yanbing LIU, Tiancang ZHANG, and Chuanchen ZHANG. Structure and mechanical properties of tc4/tc17 linear friction welding joint [j]. *Transactions of the China Welding Institution*, 10, 2012.
- [25] Wen-Ya Li, Tiejun Ma, and Siqian Yang. Microstructure evolution and mechanical properties of linear friction welded ti-5al-2sn-2zr-4mo-4cr (ti17) titanium alloy joints. *Advanced Engineering Materials*, 12(12):35–43, 2010. doi: 10.1002/adem.200900185. URL <http://onlinelibrary.wiley.com/doi/abs/10.1002/adem.200900185>.
- [26] E. Dalgaard, P. Wanjara, J. Gholipour, X. Cao, and J.J. Jonas. Linear friction welding of a near- β titanium alloy. *Acta Materialia*, 60(2):770 – 780, 2012. ISSN 1359-6454. doi: <https://doi.org/10.1016/j.actamat.2011.04.037>. URL <http://www.sciencedirect.com/science/article/pii/S1359645411002898>.
- [27] Priti Wanjara, Elvi Dalgaard, Javad Gholipour, Xinjin Cao, Jonathan Cuddy, and John J. Jonas. Effect of pre- and post-weld heat treatments on linear friction welded ti-5553. *Metallurgical and Materials Transactions A*, 45(11):5138–5157, Oct 2014. ISSN 1543-1940. doi: 10.1007/s11661-014-2475-y. URL <https://doi.org/10.1007/s11661-014-2475-y>.
- [28] Vadim Ivanovich Vill. *Friction welding of metals*, volume 1. American Welding Society; trade distributor: Reinhold Pub. Co., 1962.
- [29] A. Vairis and M. Frost. High frequency linear friction welding of a titanium alloy. *Wear*, 217(1): 117 – 131, 1998. ISSN 0043-1648. doi: [https://doi.org/10.1016/S0043-1648\(98\)00145-8](https://doi.org/10.1016/S0043-1648(98)00145-8). URL <http://www.sciencedirect.com/science/article/pii/S0043164898001458>.
- [30] I. Bhamji, M. Preuss, P. L. Threadgill, and A. C. Addison. Solid state joining of metals by linear friction welding: a literature review. *Materials Science and Technology*, 27(1):2–12, 2011. doi: 10.1179/026708310X520510. URL <https://doi.org/10.1179/026708310X520510>.
- [31] Wenya Li, Achilles Vairis, Michael Preuss, and Tiejun Ma. Linear and rotary friction welding review. *International Materials Reviews*, 61(2):71–100, 2016. doi: 10.1080/09506608.2015.1109214. URL <https://doi.org/10.1080/09506608.2015.1109214>.
- [32] Wenya Li, Juandi Suo, Tiejun Ma, Yan Feng, and KeeHyun Kim. Abnormal microstructure in the weld zone of linear friction welded ti6.5al3.5mo1.5zr0.3si titanium alloy joint and its influence on joint properties. *Materials Science and Engineering:A*, 599:38 – 45, 2014. ISSN 0921-5093. doi: <https://doi.org/10.1016/j.msea.2014.01.071>. URL <http://www.sciencedirect.com/science/article/pii/S0921509314001026>.

- [33] P. Wanjara and M. Jahazi. Linear friction welding of ti-6al-4v: Processing, microstructure, and mechanical-property inter-relationships. *Metallurgical and Materials Transactions A*, 36(8):2149–2164, 2005. ISSN 1543-1940. doi: 10.1007/s11661-005-0335-5. URL <https://doi.org/10.1007/s11661-005-0335-5>.
- [34] M. Y. Amegadzie, O. T. Ola, O.A. Ojo, P. Wanjara, and MC. Chaturvedi. On liquation and liquid phase oxidation during linear friction welding of nickel-base in738 and cmsx superalloys. In *Superalloys 2012*, pages 587–594. John Wiley & Sons, Ltd, 2012. ISBN 9781118516430. doi: 10.1002/9781118516430.ch65. URL <https://onlinelibrary.wiley.com/doi/abs/10.1002/9781118516430.ch65>.
- [35] Simon Bray. Method of linear friction welding, 2013. Pub. No.: US 2013/0011681 A1.
- [36] P. S. Effertz, F. Fuchs, and N. Enzinger. Modelling the flash formation of linear friction welded 30crnimo8 high strength steel chains. *The International Journal of Advanced Manufacturing Technology*, 92(5):2479–2486, Sep 2017. ISSN 1433-3015. doi: 10.1007/s00170-017-0338-6. URL <https://doi.org/10.1007/s00170-017-0338-6>.
- [37] Shude Ji, Yue Wang, Jianguang Liu, Xiangchen Meng, Jun Tao, and Tiancang Zhang. Effects of welding parameters on material flow behavior during linear friction welding of ti6al4v titanium alloy by numerical investigation. *The International Journal of Advanced Manufacturing Technology*, 82(5):927–938, Feb 2016. ISSN 1433-3015. doi: 10.1007/s00170-015-7408-4. URL <https://doi.org/10.1007/s00170-015-7408-4>.
- [38] Anthony R. McAndrew, Paul A. Colegrove, Adrian C. Addison, Bertrand C.D. Flipo, and Michael J. Russell. Modelling the influence of the process inputs on the removal of surface contaminants from ti6al4v linear friction welds. *Materials & Design*, 66:183 – 195, 2015. ISSN 0261-3069. doi: <https://doi.org/10.1016/j.matdes.2014.10.058>. URL <http://www.sciencedirect.com/science/article/pii/S0261306914008462>.
- [39] R. Turner, J.-C. Gebelin, R.M. Ward, and R.C. Reed. Linear friction welding of ti6al4v: Modelling and validation. *Acta Materialia*, 59(10):3792 – 3803, 2011. ISSN 1359-6454. doi: <https://doi.org/10.1016/j.actamat.2011.02.028>. URL <http://www.sciencedirect.com/science/article/pii/S1359645411001224>.
- [40] F. Rotundo, A. Marconi, A. Morri, and A. Ceschini. Dissimilar linear friction welding between a sic particle reinforced aluminum composite and a monolithic aluminum alloy: Microstructural, tensile and fatigue properties. *Materials Science and Engineering:A*, 559:852

- 860, 2013. ISSN 0921-5093. doi: <https://doi.org/10.1016/j.msea.2012.09.033>. URL <http://www.sciencedirect.com/science/article/pii/S0921509312013470>.
- [41] Yingping Ji and Sujun Wu. Study on microstructure and mechanical behavior of dissimilar titanium friction welds. *Materials Science and Engineering:A*, 596:32 – 40, 2014. ISSN 0921-5093. doi: <https://doi.org/10.1016/j.msea.2013.10.005>. URL <http://www.sciencedirect.com/science/article/pii/S0921509313011003>.
- [42] ASTM E384-17. E384-17. *Standard Test Method for Microindentation Hardness of Materials*, ASTM International, West Conshohocken, PA, 2017., 2017. doi: 10.1520/E0384-17. URL <http://www.astm.org/cgi-bin/resolver.cgi?E384>.
- [43] ASTM E8/E8M-16a. E8. *Standard Test Methods for Tension Testing of Metallic Materials*, 2016.
- [44] ASTM E 466-07. 466-07. *Standard Practice for Conducting Force Controlled Constant Amplitude Axial Fatigue Tests of Metallic Materials*, 2007.
- [45] Juan Manuel García and Thilo Frank Morgeneyer. On the use of stereo digital image correlation for the alignment of fatigue testing machines in accordance with international standards. *In preparation*, 2020.
- [46] ASTM E1820-08. E1820-08. *Standard Test Method for Measurement of Fracture Toughness*, 2008.
- [47] S. L. Semiatin, V. Seetharaman, and I. Weiss. The thermomechanical processing of alpha/beta titanium alloys. *JOM*, 49(6):33–39, Jun 1997. ISSN 1543-1851. doi: 10.1007/BF02914711. URL <https://doi.org/10.1007/BF02914711>.
- [48] Dorick Ballat-Durand, Salima Bouvier, Marion Risbet, and Wolfgang Pantleon. Through analysis of the microstructure changes during linear friction welding of the near- α titanium alloy Ti-6Al-2Sn-4Zr-2Mo (Ti6242) towards microstructure optimization. *Materials Characterization*, 151:38 – 52, 2019. ISSN 1044-5803. doi: <https://doi.org/10.1016/j.matchar.2019.02.027>. URL <http://www.sciencedirect.com/science/article/pii/S1044580318332443>.
- [49] Vinod Deshmukh, Raju Kadam, and Suhas S. Joshi. Removal of alpha case on titanium alloy surfaces using chemical milling. *Machining Science and Technology*, 21(2):257–278, 2017. doi: 10.1080/10910344.2017.1284558. URL <https://doi.org/10.1080/10910344.2017.1284558>.

- [50] L. Huang, P. Kinnell, and P.H. Shipway. Removal of heat-formed coating from a titanium alloy using high pressure waterjet: Influence of machining parameters on surface texture and residual stress. *Journal of Materials Processing Technology*, 223:129 – 138, 2015. ISSN 0924-0136. doi: <https://doi.org/10.1016/j.jmatprotec.2015.03.053>. URL <http://www.sciencedirect.com/science/article/pii/S0924013615001569>.
- [51] Chuan-chen Zhang, Tian-cang Zhang, Ya-juan Ji, and Ji-hua Huang. Effects of heat treatment on microstructure and microhardness of linear friction welded dissimilar ti alloys. *Transactions of Nonferrous Metals Society of China*, 23(12):3540 – 3544, 2013. ISSN 1003-6326. doi: [https://doi.org/10.1016/S1003-6326\(13\)62898-8](https://doi.org/10.1016/S1003-6326(13)62898-8). URL <http://www.sciencedirect.com/science/article/pii/S1003632613628988>.
- [52] M. Wojtaszek, T. Sleboda, A. Czulak, G. Weber, and W.A. Hufenbach. Quasi-static and dynamic tensile properties of ti-6al-4v alloy. *Archives of Metallurgy and Materials*, 58(4):1261 – 1265, 2013. URL <https://content.sciendo.com/view/journals/amm/58/4/article-p1261.xml>.
- [53] D. Lunt, J. Quinta da Fonseca, D. Rugg, and M. Preuss. Microscopic strain localisation in ti-6al-4v during uniaxial tensile loading. *Materials Science and Engineering:A*, 680:444 – 453, 2017. ISSN 0921-5093. doi: <https://doi.org/10.1016/j.msea.2016.10.099>. URL <http://www.sciencedirect.com/science/article/pii/S0921509316313260>.
- [54] Christophe Buirette, Julitte Huez, Nathalie Gey, Alain Vassel, and Eric Andrieu. Study of crack propagation mechanisms during charpy impact toughness tests on both equiaxed and lamellar microstructures of ti-6al-4v titanium alloy. *Materials Science & Engineering:A*, 618: 546 – 557, 2014. ISSN 0921-5093. doi: <https://doi.org/10.1016/j.msea.2014.09.048>. URL <http://www.sciencedirect.com/science/article/pii/S0921509314011538>.
- [55] W.G. Burgers. On the process of transition of the cubic-body-centered modification into the hexagonal-close-packed modification of zirconium. *Physica*, 1(7):561 – 586, 1934. ISSN 0031-8914. doi: [https://doi.org/10.1016/S0031-8914\(34\)80244-3](https://doi.org/10.1016/S0031-8914(34)80244-3). URL <http://www.sciencedirect.com/science/article/pii/S0031891434802443>.
- [56] O.P. Karasevskaya, O.M. Ivasishin, S.L. Semiatin, and Yu.V. Matviychuk. Deformation behavior of β -titanium alloys. *Materials Science & Engineering:A*, 354(1):121 – 132, 2003. ISSN 0921-5093. doi: [https://doi.org/10.1016/S0921-5093\(02\)00935-8](https://doi.org/10.1016/S0921-5093(02)00935-8). URL <http://www.sciencedirect.com/science/article/pii/S0921509302009358>.

- [57] E. Aeby-Gautier, A. Settefrati, F. Bruneseaux, B. Appolaire, B. Denand, M. Dehmas, G. Geandier, and P. Boulet. Isothermal α formation in β metastable titanium alloys. *Journal of Alloys and Compounds*, 577:S439 – S443, 2013. ISSN 0925-8388. doi: <https://doi.org/10.1016/j.jallcom.2012.02.046>. URL <http://www.sciencedirect.com/science/article/pii/S0925838812003088>. SI :ICOMAT2011.
- [58] TW Duerig, RM Middleton, GT Terlinde, and JC Williams. Stress Assisted Transformation in Ti-10V-2Fe-3Al. Technical report, Carnegie-Mellon University Pittsburgh PA department of Metallurgy and Materials Science, 1980.
- [59] ESK Menon, JK Chakravartty, SL Wadekar, and S Banerjee. Stress induced martensitic transformation in ti-20v. *Le Journal de Physique Colloques*, 43(C4):C4-321, 1982.
- [60] A. Chamanfar, M. Jahazi, J. Gholipour, P. Wanjara, and S. Yue. Suppressed liquation and microcracking in linear friction welded waspaloy. *Materials & Design (1980-2015)*, 36:113 – 122, 2012. ISSN 0261-3069. doi: <https://doi.org/10.1016/j.matdes.2011.11.007>. URL <http://www.sciencedirect.com/science/article/pii/S0261306911007679>. Sustainable Materials, Design and Applications.
- [61] Juan Manuel García, Fabrice Gaslain, and Thilo F. Morgeneyer. On the effect of a thermal treatment on the tensile and fatigue properties of weak zones of similar Ti17 linear friction welded joints and parent material. *Materials Characterization*, 2020. (in preparation).